Editors' Suggestion

Stability of multiferroic phase and magnetization-polarization coupling in Y-type hexaferrite crystals

V. Kocsis,[1] T. Nakajima,[1] M. Matsuda,[2] A. Kikkawa,[1] Y. Kaneko,[1] J. Takashima,[1,3] K. Kakurai,[1,4] T. Arima,[1,5] Y. Tokunaga,[1,5] Y. Tokura,[1,6] and Y. Taguchi[1]

[1]*RIKEN Center for Emergent Matter Science (CEMS), Wako, Saitama 351-0198, Japan*

[2]*Neutron Scattering Division, Oak Ridge National Laboratory, Oak Ridge, Tennessee 37831, USA*

[3]*Venture Lab Tokyo, NGK Spark Plug Co., Ltd., Minato-ku, Tokyo 108-8243, Japan*

[4]*Neutron Science and Technology Center, Comprehensive Research Organization for Science and Society (CROSS), Tokai, Ibaraki 319-1106, Japan*

[5]*Department of Advanced Materials Science, University of Tokyo, Kashiwa 277-8561, Japan*

[6]*Tokyo College and Department of Applied Physics, University of Tokyo, Hongo, Tokyo 113-8656, Japan*

(Received 26 November 2019; accepted 31 January 2020; published 26 February 2020)

Most of the Y-type hexaferrite materials family hosts a variety of magnetic structures as a ground state, and a multiferroic phase, termed the FE3 phase, can be stabilized by applying a magnetic (H) field. This phase has recently been found to persist even after removing the H field. The magnetoelectric properties of Y-type hexaferrites are dominated mainly by the FE3 phase via the spin-driven electric polarization (P). In the present study, the stability of the competing magnetic phases was investigated in Y-type hexaferrite compounds $Ba_{2-y}Sr_yCo_2Fe_{12-x}Al_xO_{22}$ ($x = 0.9$) with Sr-doping levels of $y = 0.8$, 1.0, and 1.2. Combining the measurements of magnetization (M), P, and neutron diffraction, we revealed the H-T magnetic phase diagrams. It was found that the stability of the multiferroic FE3 phase is greatly improved in the Sr-rich compound. At room temperature, the FE3 phase in the Ba-rich compound is fragile against the removal of the H field, while it is robust in the Sr-rich compound, even for zero-field cooling. We also investigated the interplay between P and M in the FE3 phase in the presence of both the high electric (E) and H fields, and we found that the coupling between P and M depends on the energy barrier separating the two magnetoelectric states. The energy barrier gradually decreases as the temperature is increased, leading to a reduction of the P-M coupling.

DOI: 10.1103/PhysRevB.101.075136

I. INTRODUCTION

Recent advances in the research on novel multiferroics, which have (anti)ferroic order of both electric polarization (P) and magnetization (M), have attracted great interest due to their potential for applications [1–6]. When the coupling between the P and M is strong, they can be manipulated by the application of magnetic (H) and electric (E) fields, respectively. This cross-coupling effect gives additional functionality to materials and is thus anticipated to be employed in spintronic devices. Magnetization control by E field is of particular interest, as it may combine the high reliability of magnetic devices and the capability of high-speed electric manipulation with ultralow power-consumption.

Multiferroics are often classified [7] into two groups according to the relationship between P and M. In type-I multiferroics, P typically emerges at higher temperatures and independently of the magnetic order, while in type-II multiferroics, P is produced by the spin order [8–10]. Heterostructures based on the type-I multiferroic $BiFeO_3$ have been considered to be the most promising candidates for applications for a long time, as the manipulation of magnetic domains by E field was demonstrated at room temperature [11,12]. However, in these materials the relationship between the magnetic and electric degrees of freedoms is not mutual; although the M is reversed to $-M$ by the E field, the spin-driven P is an even function of the H field [13], that is, it is not switched by the reversal of H. Among the type-II multiferroics, where the P-M coupling is considered to be stronger than in type-I materials, the vast family of hexaferrite materials with versatile structural types has gained considerable interest [4,5,14–17]. In Z-type hexaferrite materials, multiferroic phases were observed at high temperatures and in small H fields. However, despite the high stability of the multiferroic phases, the magnetoelectric response is dominated mainly by a contribution that shows a symmetric H-field dependence [18,19] (although the existence of a minor component with an antisymmetric H-field dependence has recently been identified [19]). In materials with symmetric P-H and M-E field dependence [17], the reversal of P and M upon the reversal of the H and E fields is not expected. In Y-type hexaferrites, magnetoelectric responses with an antisymmetric field dependence were observed at low temperatures [20–22].

In the phase diagrams of the Y-type hexaferrites, a large variety of noncollinear magnetic phases, both incommensurate and commensurate, can be realized by chemical doping. Among them, Sr- and Al-doping in $Ba_{2-y}Sr_yM_2Fe_{12-x}Al_xO_{22}$ (M = Mg,Co,Zn) proved to be an effective way to stabilize the multiferroic phases [23–28]. This has led to the realization of M switching by E field at low temperatures [20,21].

Moreover, a stable multiferroic phase, termed the FE3 phase, was reported at room temperature in $Ba_{1.0}Sr_{1.0}Co_2Fe_{11}AlO_{22}$ [27,28]. In a previous paper [29], we reported successful control of M by E and visualization of M-domain switching by E using magnetic force microscopy in a related compound near room temperature. This motivated us to systematically study the effect of Sr-doping on the magnetoelectric phases and responses in $Ba_{2-y}Sr_yCo_2Fe_{12-x}Al_xO_{22}$. In this paper, we report the stability of the multiferroic phases with the change in the Ba/Sr ratio, and we investigate the robustness of P-M coupling of the multiferroic phase.

II. EXPERIMENTAL METHODS

Single-crystalline Y-type hexaferrites $Ba_{2-y}Sr_yCo_2Fe_{12-x}Al_xO_{22}$ with $x = 0.9$ and $y = 0.8$, 1.0, and 1.2 were grown by the laser floating-zone method [30]. A polycrystalline precursor was prepared by solid-state reaction of stoichiometric amounts of $SrCO_3$, $BaCO_3$, Co_3O_4, Fe_2O_3, and Al_2O_3 in air at 1150 °C for 24 h. The resulting product was pressed into rods and sintered for 14 h. Single crystals ∼10 cm in length were grown in the laser floating-zone furnace in a 10 atm oxygen atmosphere. The ingots were oriented with a backscattering Laue camera and cut into disks with ac surfaces.

Resistivity of the as-grown samples is too low for high-temperature magnetoelectric measurements [29]. To increase the resistivity, we followed Ref. [31] and performed a high-pressure O_2 annealing. The cut pieces were sealed in quartz tubes and annealed in 10 atm O_2 at 1000 °C for 100 h using Ag_2O as an oxygen source.

Neutron diffraction measurements were carried out for the O_2-annealed single crystals at the triple-axis neutron spectrometer (PTAX) in the High Flux Isotope Reactor of Oak Ridge National Laboratory. The $(H, 0, L)$ plane was selected as a scattering plane, while the H field was applied perpendicular to the c axis (see Fig. 1).

For P-H and M-E measurements, single crystals with ac faces were polished and coated with Au/Pt electrodes. The E and H fields were applied perpendicular to each other and to the c axis ($\mathbf{E} \perp \mathbf{H}$; $\mathbf{E}, \mathbf{H} \perp c$). The P was obtained by measuring and integrating the displacement current with an electrometer (Keithley 6517A) while the H field was swept in a Physical Property Measurement System (PPMS, Quantum Design). The M-T and M-H measurements without E field were carried out in a Magnetic Property Measurement System (MPMS-3, Quantum Design). The M-E and M-H measurements under E field were performed by using a magnetometer (MPMS-XL, Quantum Design), while an electrometer (6517A, Keithley) was used as a voltage source. Prior to the measurements, a single-domain magnetoelectric state was prepared by the application of $E_0 = +5$ MV/m and $H_0 = +50$ kOe fields in the $\mathbf{E} \perp \mathbf{H}$; $\mathbf{E}, \mathbf{H} \perp c$ arrangement at the same temperature as the respective measurement temperature.

III. STRUCTURE AND COMPETING MAGNETIC PHASES

The Y-type hexaferrites $Ba_{2-y}Sr_yCo_2Fe_{12-x}Al_xO_{22}$ have a large structural unit cell (space group $R\bar{3}m$) with hexagonal lattice constants $a = a' \approx 5.8$ Å and $c \approx 43.3$ Å, as shown in Fig. 1(a). Fe^{3+}/Co^{2+} and Fe^{3+}/Al^{3+} ions are in either tetrahedral or octahedral ligand coordination [16,32]. The magnetic structure is known to be greatly simplified by employing a block-spin approximation [5,33–36]. The magnetic moments of the Fe^{3+}/Co^{2+} ions constitute spin-blocks with small (S^S) and large (S^L) net magnetizations. Although the precise order within the blocks is unknown, they probably have a nearly collinear ferrimagnetic order [33–35]. The complete magnetic structure is composed of alternate stacks of these two spin-blocks along the c axis.

In the Y-type hexaferrites, the Al-doping selectively replaces the Fe^{3+} ions at the octahedral sites [15,37]. By weakening both the superexchange interactions and the easy-plane anisotropy, the Al-doping was found to suppress the coplanar incommensurate phases [26]. By contrast, as the Ba and Sr ions are located in between the S^S and S^L spin blocks, substituting Sr for Ba alters the Fe-O-Fe bond angles connecting the two blocks [33–35]. This leads to a change in the rotation angle between S^S and S^L block-spins, as well as to the prevalence of noncollinear magnetic structures with helical modulation. By doping with Al and Sr, we have access to different microscopic interactions, and it is possible to stabilize a variety of noncollinear magnetic phases.

Figures 1(b) and 1(d) illustrate the relevant magnetic structures to this study, namely the collinear ferrimagnetic phase (FiM), proper screw (PS), alternating longitudinal conical (ALC), as well as multiferroic FE2′ and FE3 phases. In this paper, we follow the nomenclature introduced in Ref. [23]. The magnetic phases were identified using the representative $(0, 0, q)$ magnetic modulation wave vectors in the neutron diffraction profiles measured along the $(0, 0, L)$ and $(1, 0, L)$ lines [5,28,36]. In the present study, we focused on the L ranges of $6 \leqslant L \leqslant 9$ and $1 \leqslant L \leqslant 4$ in the former and latter line scans, respectively. The assignment of the magnetic phases to the q modulation wave numbers is summarized in Table I, while the details are discussed in the Supplemental Material [38]. The FiM phase is a collinear phase with uniform magnetization ($q = 0$) where S^S and S^L point to opposite directions, which can be viewed as a parent structure of all other phases. The PS phase has an incommensurate spiral order ($q = q_{IC}$), with the magnetic moments confined within the ab plane due to the easy-plane anisotropy. The ALC phase has an incommensurate ab-plane component ($q = q_{IC}$) similar to the PS phase, but the c-axis component of the moments shows commensurate modulation with $q = 3/2$ along the c axis. In the FE2′ structure ($q = 3/4$), the S^L block-spins have a fourfold modulation [36], which hosts ferroelectric polarization.

Among these magnetically ordered phases, the multiferroic FE3 phase has prominent significance as it appears in many Y-type hexaferrites and dominates the magnetoelectric properties [5,27,28,36]. The FE3 can be viewed as a double-fan structure with S^L and S^S lying within the ab and ac planes, respectively, as shown in Fig. 1(b). The FE3 structure can be also considered [28] as being composed of a staggered collinear ferrimagnetic component and an elliptical cycloidal one, which are parallel and perpendicular to the net M, respectively. The ferroelectric polarization is associated with the cycloidal component and emerges due to the spin-current mechanism [8,39,40], perpendicular to both the net

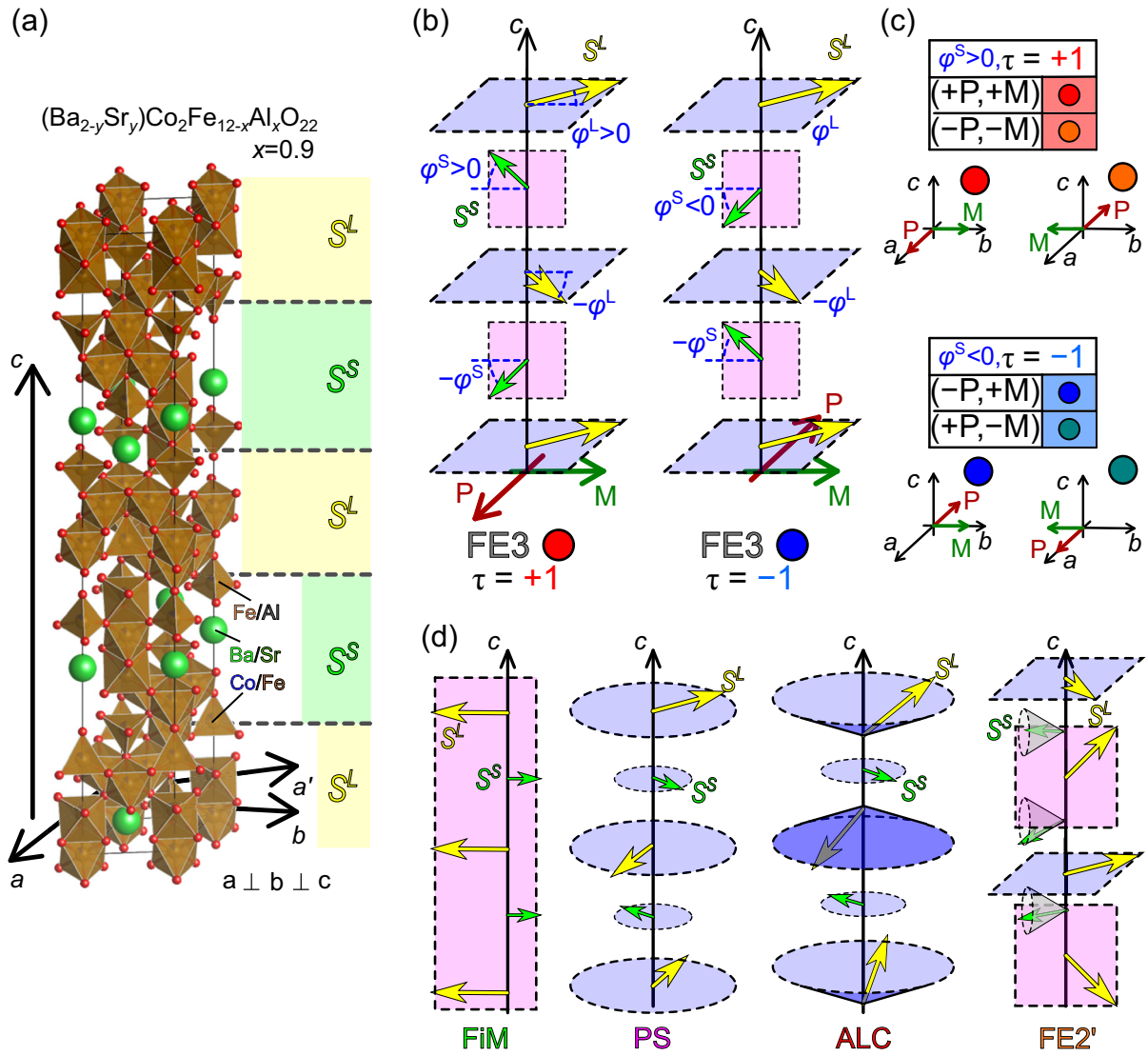

FIG. 1. (a) The hexagonal unit cell of the Y-type hexaferrite $Ba_{2-y}Sr_yCo_2Fe_{12-x}Al_xO_{22}$ ($x = 0.9$), shown together with alternating layers of the S^L and S^S spin-blocks. While the a, a', and c lattice vectors span the hexagonal basis, we define the orthogonal axis $b(\propto c \times a)$ for the convenient description of the experiments. (b) The block-spins in the FE3 phase form a double-fan structure, where the S^L and S^S are confined within the orthogonal ab and ac planes, respectively. The spin-driven **P** is induced perpendicular to the net **M**, which can rotate around the c axis almost freely due to the negligible anisotropy within the ab plane. The S^L and S^S block-spins are specified by the angles φ^L and φ^S, respectively, as indicated in the right panel. The phase between the S^L and S^S spin-blocks is different in the two independent magnetoelectric states of the FE3 phase, labeled as $\tau = +1$ and -1. $\varphi^L > 0$ is assumed without losing generality, and then the $\tau = +1$ magnetoelectric state has $\varphi^S > 0$, while the $\tau = -1$ state has $\varphi^S < 0$. (c) The four independent $(\pm P, \pm M)$ states of the FE3 phase with $\mathbf{P} \perp \mathbf{M}$; $\mathbf{P}, \mathbf{M} \perp c$ are classified according to the P-M coupling. The $(+P, +M)$ and $(-P, -M)$ states are essentially the same states and are categorized as the $\tau = +1$ magnetoelectric state. On the other hand, $(-P, +M)$ and $(+P, -M)$ states are classified together to form the $\tau = -1$ state. The magnetoelectric state is selected by the application of high electric (E) and magnetic (H) fields in the $\mathbf{E} \perp \mathbf{H}$; $\mathbf{E}, \mathbf{H} \perp c$ configuration. (d) Schematic illustration of the collinear ferrimagnetic (FiM), proper screw (PS), alternating longitudinal conical (ALC), and the FE2′ phases. Note that only the illustration for the FE2′ phase is compressed along the c axis.

magnetization and the c axis ($\mathbf{P}, \mathbf{M} \perp c$ and $\mathbf{P} \perp \mathbf{M}$). In the presence of the P-M coupling, the four independent $\pm M$ and $\pm P$ states are reduced to two magnetoelectric states, labeled as $\tau = +1$ and -1, as depicted in Figs. 1(b) and 1(c). The $\tau = +1$ magnetoelectric state means that the $+P$ and $-P$ states are coupled to the $+M$ and $-M$ states, respectively. On the other hand, the $\tau = -1$ magnetoelectric state indicates the coupling between the $+P$ and $-M$ states, or $-P$ and $+M$ states. Here we note that due to the weak anisotropy within the ab plane [29], the M and P may rotate within the ab plane nearly freely, while keeping the relative configuration of P and M, and hence the magnetoelectric state, unchanged. In fact, this is the key for the M switching in this materials family [20,28].

The angles between S^L and M, and S^S and $-M$, are denoted as φ^L and φ^S, respectively, as shown in Fig. 1(b). The two magnetoelectric states of the FE3 phase differ in the relative phase between the S^L and S^S spin-blocks. For a fixed phase of

TABLE I. Magnetic phases and their corresponding modulation vectors as well as the magnetic reflections used to identify the phases.

Phase	Wave vector	Reflections
FiM	$q = 0$	$(0, 0, 9)$, $(1, 0, 4)$
PH	$q = q_{IC}$	$(0, 0, 9 \pm q_{IC})$, $(1, 0, 4 \pm q_{IC})$
ALC	$q = q_{IC}$, $q = 3/2$	$(0, 0, 9 \pm q_{IC})$, $(1, 0, 4 \pm q_{IC})$, $(1, 0, 4 \pm 3/2)$
FE2′	$q = 3/4$, $q = 0$	$(0, 0, 9)$, $(1, 0, 4)$, $(0, 0, 9 \pm 3/4)$, $(1, 0, 4 \pm 3/4)$
FE3	$q = 3/2$, $q = 0$	$(0, 0, 9)$, $(1, 0, 4)$, $(0, 0, 9 \pm 3/2)$, $(1, 0, 4 \pm 3/2)$

the large spin-block ($\varphi^{L} > 0$), the magnetoelectric state $\tau = +1$ corresponds to $\varphi^{S} > 0$, while the $\tau = -1$ state has an opposite sign $\varphi^{S} < 0$. The magnetoelectric states can be changed with each other by interchanging the signs of either of the φ^{L} or φ^{S} angles. The φ^{L} and φ^{S} angles are governed by the interplay between the exchange couplings and anisotropies, thus they depend on the chemical composition, temperature, and magnetic field. The FE3 phase can be deformed into the FiM phase by tuning the angles to zero ($\varphi^{L} = 0$, $\varphi^{S} = 0$).

A. Phase diagram in the zero-field-cooled state

In this section, we first describe the magnetic phases of the compound with equal Ba/Sr ratio ($y = 1.0$) using the magnetization data in the low-field-cooled state and the neutron diffraction data collected for a zero-field-cooled (ZFC) state in Fig. 2. Then, we proceed to compare the ZFC phase diagrams of the other two compounds and discuss the impact of Sr-doping.

The ZFC magnetic phase diagram of the $y = 1.0$ compound is presented in Fig. 2(b), which was deduced from the magnetization and neutron diffraction data shown in Figs. 2(e), 2(h), and 2(k). Corresponding neutron diffraction profiles measured along the $(0, 0, L)$ line are shown in Fig. S1 of the Supplemental Material at selected temperatures. The $y = 1.0$ compound develops a long-range collinear FiM order below $T_{C1} = 470$ K, which is identified by the onset of M for $H \perp c$ ($M_{\perp c}$) in Fig. 2(e) as well as the increase in the integrated intensities of the $(0, 0, 9)$ and $(1, 0, 4)$ peaks, which are denoted as $q = 0$ in Figs. 2(h) and 2(k). At $T_{C2} = 420$ K, the FiM phase is turned into the coplanar PS phase, which is indicated by the rapid decrease in $M_{\perp c}$, the emergence of magnetic satellite peaks with $q = q_{IC}$, and the decrease in the intensities of the $(0, 0, 9)$ and $(1, 0, 4)$ peaks. Besides the incommensurate magnetic satellite peak, a commensurate modulation vector $q = 3/2$ with small intensity also appears. This suggests the emergence of the FE3 phase coexisting with the PS order as a minority phase. Finally, around $T_{C3} = 280$ K, $M_{\perp c}$ shows a gradual increase, while the M for $H \parallel c$ ($M_{\parallel c}$) exhibits a kink. The ALC phase below T_{C3} is identified by the $q = q_{IC}$ magnetic peak as well as the emergence of the magnetic $q = 3/2$ peak along the $(1, 0, L)$ line, as shown in Fig. 2(k) and Table I. Here we note that the intensity change across the boundaries between the ALC, PS, and FiM phases is gradual and continuous, suggesting the second-order nature of the phase transitions.

The magnetic phase diagram of the Ba-rich compound ($y = 0.8$) is rather similar to that of the $y = 1.0$ compound, as shown in Fig. 2(a), and there are only minor differences. The onset of the FiM order is shifted toward higher temperature ($T_{C1} = 485$ K) accompanied by the enhancement of the $M_{\perp c}$, while $M_{\parallel c}$ is almost unchanged. As compared to the $y = 1.0$ compound, the intensity of the $q = 3/2$ magnetic peak along the $(0, 0, L)$ line is much reduced, except for a narrow temperature region around T_{C2} [Fig. 2(g)]; the FE3 phase is almost completely destabilized in this compound. The boundaries between the FiM, PS, and ALC phases (T_{C2} and T_{C3}) are roughly the same as those in the $y = 1.0$ compound.

The Sr-rich compound ($y = 1.2$) has a substantially different ZFC phase diagram from the other two compounds, as reproduced in Fig. 2(c) from Ref. [29]. The most important difference is the coexistence of multiple magnetic phases, which was verified at $T = 295$ K by using magnetic force microscopy in the earlier study [29]. Besides the FiM order, the multiferroic FE3 phase with $q = 3/2$ appears at $T_{C1} = 450$ K, as shown in Figs. 2(i) and 2(l). While the FiM phase is replaced by the PS and FE2′ phases at $T_{C2} = 400$ K, the latter of which is identified with the $q = 3/4$ magnetic reflection, the FE3 phase persists down to low temperatures. Notably, $M_{\perp c}$ does not decrease substantially below T_{C2} as compared with $y = 0.8$ and 1.0 compounds, which is an indication of the stable FE2′ and FE3 phases. Finally, at $T_{C3} = 300$ K the PS is replaced by the ALC phase. The increase in the $M_{\perp c}$ below T_{C3} is probably related to the FE2′ and FE3 phases rather than to the ALC phase.

The phase-transition temperatures of all three compounds are summarized in Table II, while the Ba/Sr-ratio dependence of the q_{IC} in the incommensurate ALC and PS phases is shown in Fig. S2. The q_{IC} has a nonmonotonous temperature dependence, and the periodicity of the modulation is increased as the Sr-doping level is increased. To give a more intuitive picture for the effect of Sr-doping on q_{IC}, we note that the turn angle between two neighboring S^{L} block-spins along the c axis is increased from 95° for $y = 0.8$ to 120° for $y = 1.2$, at $T = 300$ K.

B. Magnetic phases in the $H \perp c$ field

In the previous section, we discussed the ZFC magnetic phase diagram of Sr-doped Y-type hexaferrites. In this section, we proceed to discuss the phase diagram as a function of applied field ($\mathbf{H} \perp c$) at room temperature. Following the temperature-dependent phase diagrams, we start with the description for the $y = 1.0$, then we compare the other two compounds with lower and higher Sr-doping levels.

The $H_{\perp c}$ field-dependent neutron scattering measurement for the $y = 1.0$ compound was started from the ZFC state at $T = 295$ K. In agreement with the earlier reports on similar compounds [27,28,37], the PS phase with $q_{IC} = 0.89$ modulation is stabilized in the initial ZFC state, as shown

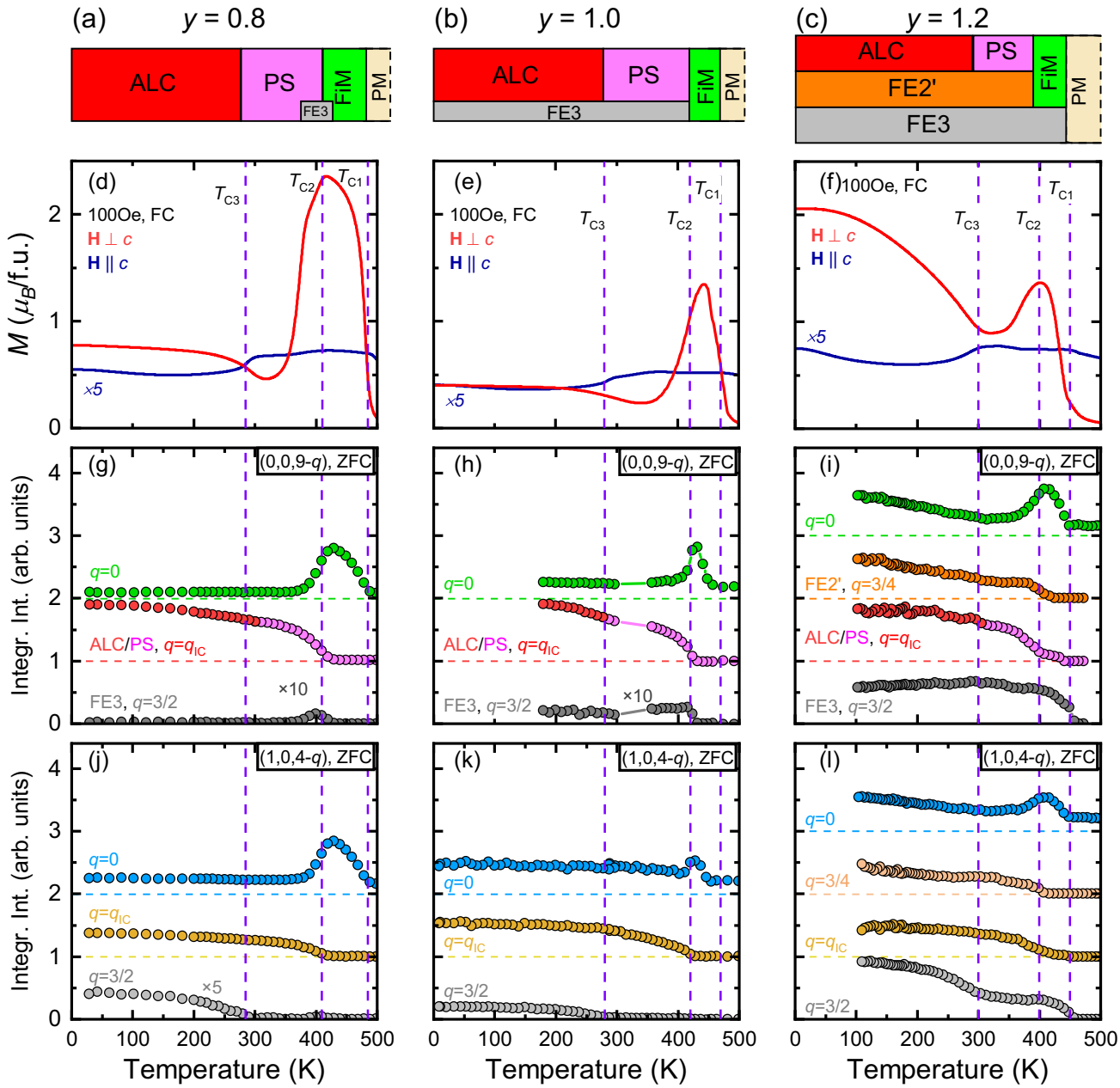

FIG. 2. (a)–(c) Magnetic phase diagrams of $Ba_{2-y}Sr_yCo_2Fe_{12-x}Al_xO_{22}$ ($x = 0.9$) with different Ba/Sr ratios, (a) $y = 0.8$, (b) $y = 1.0$, and (c) $y = 1.2$ in the zero-field-cooled (ZFC) state. The magnetic structures for respective phases are illustrated in Fig. 1. (d)–(f) Temperature dependence of the low-field-cooled (FC) magnetization $M_{\perp c}$ and $M_{\parallel c}$ for $\mathbf{H} \perp c$ and $\mathbf{H} \parallel c$, respectively, measured in the 100 Oe field. Note that the $M_{\parallel c}$ is multiplied by 5 for better visibility. (g)–(l) Integrated intensities of the neutron diffraction peaks for $q = 0$, 3/4, 3/2, and q_{IC} measured in the ZFC runs. The scattering intensities were measured along the (0, 0, 9-q) and (1, 0, 4-q) lines, respectively, for the data shown in panels (g)–(i) and panels (j)–(l).

in Fig. 3. A small peak is observed at $L = 7.5$ ($q = 3/2$) in Fig. 3, which indicates the presence of the FE3 phase as a minority phase. Upon the application of H field perpendicular to the c axis, the magnetic reflections with q_{IC} disappear and the intensity at $L = 7.5$ ($q = 3/2$) significantly increases for $H = 3$ kOe. According to more a detailed field dependence [see Figs. 4(h), 4(k), and 4(n)], the PS phase is completely replaced by the FE3 phase at around $H = 0.9$ kOe. When the $H_{\perp c}$ field is removed, the intensity of the $q = 3/2$ reflection decreases to almost half, compared to that at 3 kOe, that is, the FE3 phase is only partially preserved. Besides the change in the $q = 3/2$ reflection, a new, asymmetric magnetic peak emerges around $q = 0.77$, which is close to the $q = 3/4$ of the FE2′ phase. The change in the shape and position of the magnetic peak suggests the mixture of the coexistent PS and FE2′ phases, rather than the restoration of the PS phase with a field-history-dependent, slightly different q_{IC} modulation vector. The analysis of the scattering intensity in terms of the PS and FE2′ phases is detailed in Fig. S3 [38].

The integrated intensity of representative peaks is plotted as a function of applied field in Figs. 4(h), 4(k), and 4(n). In the low-field region ($H < 1$ kOe), the field variation of the

TABLE II. T_{C1}, T_{C2}, and T_{C3} are the magnetic phase transition temperatures that separate the PM (paramagnetic), FiM (collinear ferrimagnetic), PS (proper-screw), and ALC (alternating longitudinal conical) phases, respectively. At low temperature, the FE3 phase is stabilized in the presence of a high $H_{\perp c}$ field and preserved when the field is removed. T_1 is the temperature above which the FE3 phase becomes only partially stable in the absence of the $H_{\perp c}$ field, i.e., the FE2′ and ALC/PS phases reappear. T_2 is the highest temperature where the FE3 phase can be observed after removing the $H_{\perp c}$ field.

y	T_{C1} (K)	T_{C2} (K)	T_{C3} (K)	T_1 (K)	T_2 (K)
0.8	485	410	285	200	275
1.0	470	420	280	280	340
1.2	450	400	300	280	450

integrated intensities can be attributed to the change in volume fraction of the magnetic phases, rather than deformation of the magnetic structures. The FE3, FE2′, and PS phases are therefore represented by the integrated intensities of the $q = 3/2$, $q = 3/4$, and q_{IC} magnetic reflections on the $(0, 0, L)$ line shown in Figs. 4(h), 4(k), and 4(n), respectively. When the $H_{\perp c}$ field is reversed to negative, the intensity of the $q = 3/2$ peak has its minimum exactly where the PS and FE2′ phases have their maximum intensities. Toward even higher negative H fields, the PS phase first disappears at around $H = -0.9$ kOe, then the FE2′ phase does at $H = -1.0$ kOe, and the FE3 phase is again fully stabilized. Here the FE2′ phase is stable up to higher $H_{\perp c}$ fields and occupies a larger region in the phase diagram than the PS phase. In Fig. 4(e), the field dependence of magnetization ($M_{\perp c}$) is presented. The PS phase shows a small magnetization for $H_{\perp c}$ while the FE3 phase has a large ferrimagnetic moment. The field dependence

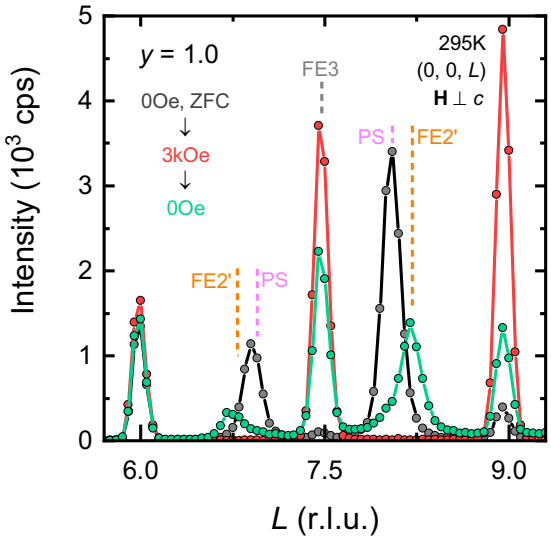

FIG. 3. Neutron diffraction profiles of the $y = 1.0$ compound measured at $T = 295$ K after ZFC, in the presence of $H = 3$ kOe applied perpendicular to the c axis, and after the removal of the H-field. Vertical dashed lines indicate the q_{IC} (of the PS phase), the $q = 3/2$ (of the FE3 phase), and the $q = 3/4$ (of the FE2′ phase) modulation vectors.

of M is understood in accordance with the neutron intensity change.

Figure 4(b) shows the magnetic phase diagram of $y = 1.0$ based on the neutron and magnetization measurements in the field-increasing run after ZFC (first line) and in the subsequent field-decreasing run (second line). The boundaries in the phase diagram were determined on the basis of the anomalies in the M-$H_{\perp c}$ measurement displayed in Fig. 4(e), while the phases were identified using the results of neutron diffraction that are shown in Figs. 4(h), 4(k), and 4(n).

As shown in Fig. 4(a), the room-temperature ZFC state of the Ba-rich compound ($y = 0.8$) is the PS phase, similar to the $y = 1.0$ compound. Details of the refinement of the neutron diffraction data are discussed in the Supplemental Material. Compared to the $y = 1.0$ compound, the PS phase is replaced by the FE3 phase more gradually between $H = 0.5$ and 1.2 kOe for the first application of magnetic field, as shown in Figs. 4(g), 4(j), and 4(m), which is accompanied by a step in the M-H curve in Fig. 4(d). Moreover, within the same magnetic field region, the intensity for the FE2′ phase also increases, showing a peak at $H = 1.0$ kOe. The disappearance of the FE2′ phase coincides with a secondary steplike feature in the M-H curve in Fig. 4(d). In the field-decreasing run, the FE3 phase is again gradually replaced by the FE2′ and PS phases. First the FE2′ phase emerges at $H = 0.7$ kOe, then the FE2′ phase partially turns into the PS phase below $H = 0.3$ kOe. In the absence of magnetic field, the FE3 phase is not stable and it reappears only below $H = -0.5$ kOe. Upon further decreasing the H field, the FE3 phase is restored from the PS and FE2′ phases at $H = -1.0$ and -1.2 kOe, respectively.

The Sr-rich compound ($y = 1.2$) hosts all three phases in its ZFC state at room temperature, as shown in Fig. 4(c). The FE3 phase is stable and the application of the $H = 0.7$ kOe field doubles the integrated intensity of the corresponding $q = 3/2$ peak, as shown in Fig 4(i). The FE2′ and PS/ALC phases are replaced by the FE3 phase at $H = 0.7$ and 1.0 kOe fields, respectively [Figs. 4(l) and 4(o)]. The phase transition is accompanied by a step in the M [Fig. 4(f)]. In the field-decreasing run, the FE3 phase is only partially replaced by the FE2′ and PS phases, similar to the $y = 1.0$ compound. The FE2′ phase reappears between $H = 0.4$ and -0.9 kOe, while the PS/ALC phase does so between the $H = 0.1$ and -0.8 kOe field range.

C. The $H_{\perp c}$-T magnetic phase diagram

Figures 5(a)–5(c) compare the $H_{\perp c}$-T magnetic phase diagrams of all three compounds in the field-increasing runs after ZFC, while Figs. 5(d)–5(f) show those obtained in the field-decreasing experiments. The phase boundaries were determined by using the anomalies in the low-field M-T data and in the field derivatives of the isothermal M-H curves. The magnetic phases were assigned according to their magnetic peaks (see Table I) observed in the neutron diffraction measurements. Isothermal M-$H_{\perp c}$ curves at selected temperatures are shown in Fig. S4.

In the compounds with $y = 0.8$ and 1.0, the FiM, PS, and ALC phases are stabilized for the ZFC below T_{C1}, T_{C2}, and T_{C3}, respectively, as shown in Figs. 5(a) and 5(b). By contrast,

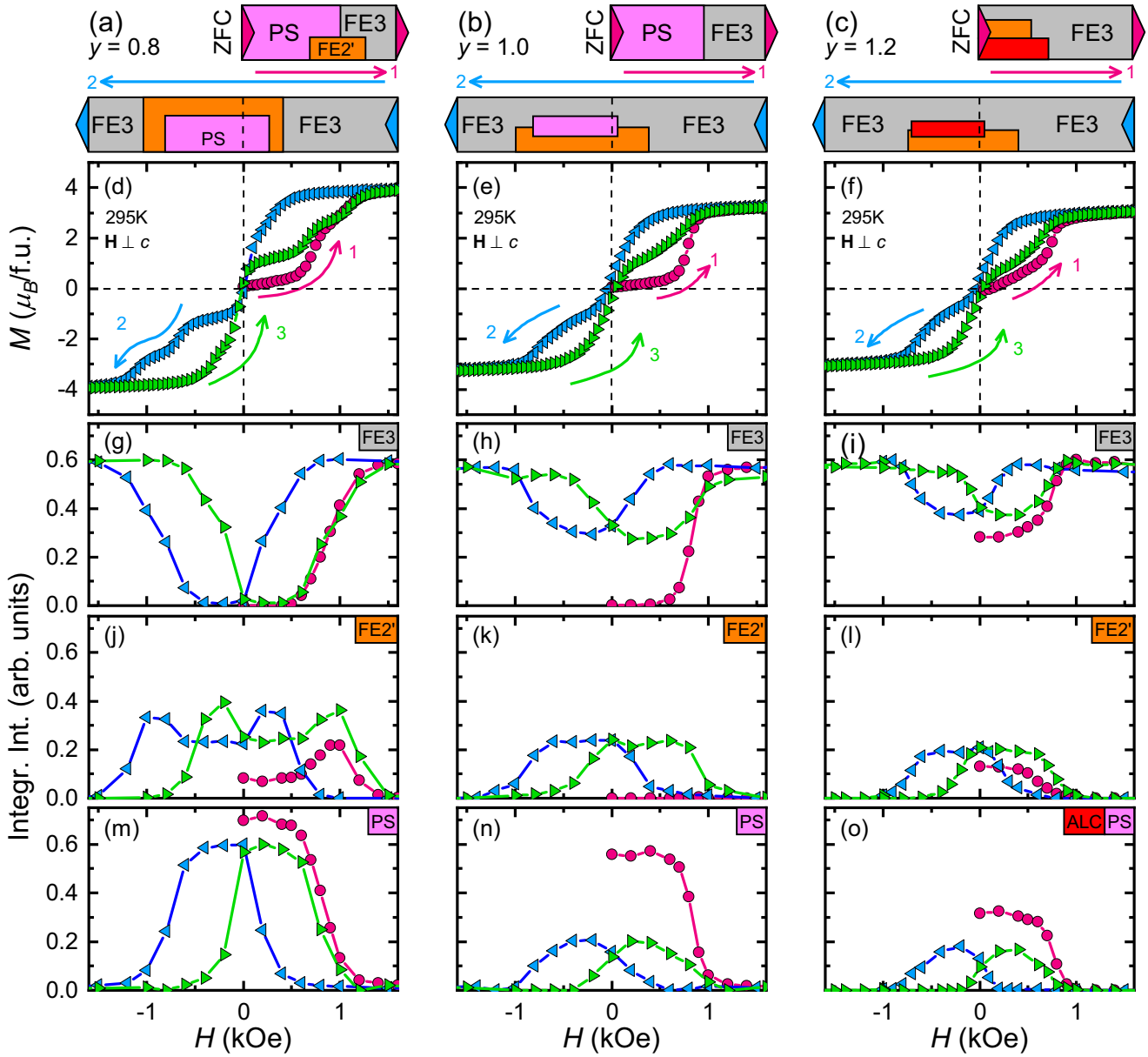

FIG. 4. (a)–(c) Field-history-dependent magnetic phase diagrams of the $Ba_{2-y}Sr_yCo_2Fe_{12-x}Al_xO_{22}$ ($x = 0.9$) hexaferrite compounds in $\mathbf{H}$ ($\perp c$) field at $T = 295$ K. The red circular symbols (1) in panels (d)–(o) denote the initial curves measured after the zero-field-cooling (ZFC) and corresponds to the first line of the phase diagrams (a)–(c). The blue left-triangular symbols (2) indicate the field-decreasing runs and are related to the second line of the $H_{\perp c}$ phase diagrams in panels (a)–(c). The green right-triangular symbols (3) represent the data collected in the field-increasing runs. (d)–(f) M-$H_{\perp c}$ measured at $T = 295$ K. (g)–(o) Magnetic-field dependence of the integrated intensities of selected magnetic reflections related to the FE3, the FE2′, and the incommensurate PS/ALC phases. The phases are represented by the $q = 3/2$, $3/4$, and q_{IC} reflections measured along the $(0, 0, L)$ line, respectively. Data for the $y = 1.2$ compound are reproduced from Ref. [29].

in the $y = 1.2$ compound the coexisting states of FiM/FE3, PS/FE2′/FE3, and ALC/FE2′/FE3 are found below the corresponding temperatures in Fig. 5(c). In each compound, the application of $H_{\perp c}$ field favors the FE3 phase exclusively. The magnitude of the $H_{\perp c}$ field to stabilize the FE3 phase decreases toward higher temperatures. For even higher $H_{\perp c}$ field in the FE3 phase, the angles between the S^S-S^S and S^L-S^L block-spin pairs gradually decrease, and the double-fan structure is finally turned into the collinear FiM structure.

In the $H_{\perp c}$-decreasing processes shown in Figs. 5(d)–5(f), the FE3 phase is restored from the high-field FiM phase. When the $H_{\perp c}$ field is removed at low temperature, the FE3 phase is fully preserved in each compound. However, in an intermediate temperature region that depends on the Sr concentration, the FE3 phase is only partially preserved, and above this temperature region the FE3 phase is unstable. In the absence of $H_{\perp c}$ field, the FE3 phase in the $y = 0.8$ compound is partially stable above $T_1 = 200$ K and unstable above $T_2 = 275$ K, as shown in Fig. 5(d). In case of the $y = 1.2$ compound [Fig. 5(f)], the FE2′ and ALC phases reappear only around $T_1 = 280$ K while the FE3 phase is partially preserved up to $T_2 = 450$ K. These temperatures representing the stability

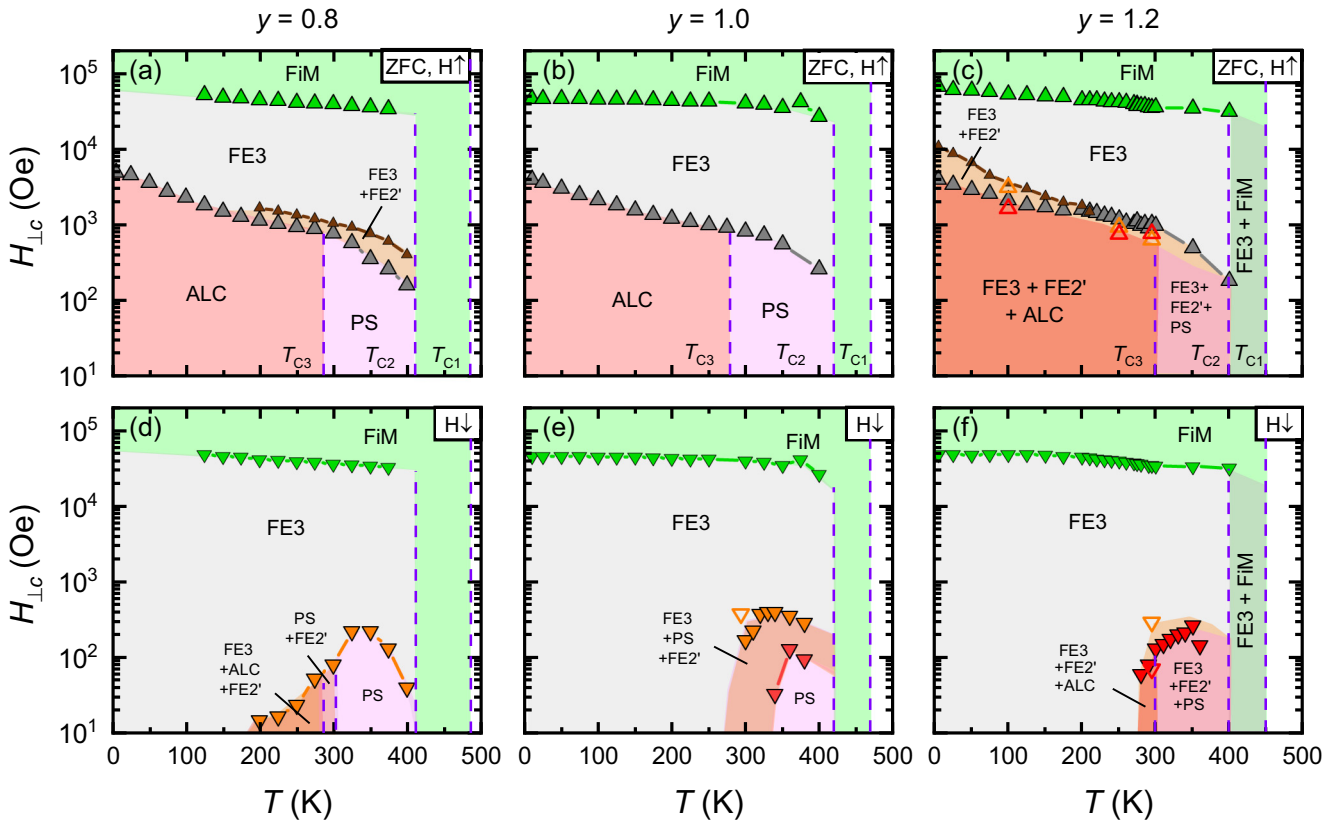

FIG. 5. The magnetic phase diagrams of the Y-type hexaferrites $Ba_{2-y}Sr_yCo_2Fe_{12-x}Al_xO_{22}$ ($x = 0.9$) with different Ba/Sr ratios for $\mathbf{H} \perp c$ configuration. Panels (a,d), (b,e), and (c,f) correspond to the samples with $y = 0.8$, 1.0, and 1.2, respectively. Panels (a)–(c) show the phase diagrams in the field-increasing runs after ZFC (upward triangles), while panels (d)–(f) are those in the field-decreasing experiments (downward triangles). The phase boundaries are determined as the anomalies in the M-H curves (closed symbols), while the identification of the phases is based on the neutron diffraction measurements (open symbols).

of the FE3 phase are summarized in Table II. Here we note that upon the reversal of the $H_{\perp c}$ field, the FE3 phase is turned into the FE2′ or ALC phase at even lower temperatures than T_1, as discussed in Ref. [29]. This suggests that the transition between the FE3 and ALC/PS phases might be related to magnetic domain walls that appear in the course of magnetization reversal; namely, the ALC/PS phase can nucleate at magnetic domain walls of the FE3 phase.

D. Summary of the magnetic phase diagram

In the Y-type hexaferrites $Ba_{2-y}Sr_yCo_2Fe_{12-x}Al_xO_{22}$ ($y = 0.8$, 1.0, and 1.2), Sr-doping stabilizes the multiferroic FE3 phase. As discussed in relation with Fig. 4, the FE3 phase is unstable, metastable, and partially stable at room temperature in the $y = 0.8$, 1.0, and 1.2 compounds, respectively. Apart from the effect on the FE3 phase, Sr-doping destabilizes the ferrimagnetic (FiM) and proper-screw (PS) phases, as their temperature regions in the phase diagram are reduced (Fig. 5). Sr-doping favors the magnetic phases with noncoplanar structure, such as the alternating longitudinal conical (ALC), FE2′, and FE3 phases. Increasing the Sr-doping gradually decreases the T_{C1}, suggesting the reduction of the strong antiferromagnetic coupling between the S^S and S^L block-spins.

The realization and stability of the FE3 phase at low temperature are discussed by using a schematic illustration of a possible free-energy diagram in Fig. 6(a) for the $y = 0.8$ compound as an example. Here we note that these free-energy diagrams are phenomenologically introduced to interpret the observed first-order transitions, based on the magnetization and neutron diffraction data, and not on a model calculation, which appears to be difficult in view of the complicated magnetic structures. The zero-field cooling (ZFC) stabilizes the incommensurate ALC phase, therefore this state has the lowest free energy in the phase space of the order parameters (represented by a horizontal axis for the purpose of simplicity). In the presence of $H_{\perp c}$ field, the free energy of the FE3 phase with a large magnetization is lowered, while the free energy of the ALC phase with a small magnetization is almost unchanged. In sufficiently large $H_{\perp c}$ field, the energy barrier separating the FE3 and ALC phases diminishes, and the incommensurate ALC phase is completely turned into the multiferroic FE3 phase. When the $H_{\perp c}$ field is removed, the energy barrier is restored, and the FE3 phase is stabilized as a metastable state [28]. At sufficiently low temperature, the energy barrier is large enough to protect the metastable FE3 phase against the thermal agitation. An increase in temperature reduces the energy barrier, making the FE3 phase less stable and the incommensurate ALC or PS phases more stable. This well accounts for the experimental observations shown in Fig. 5. As the temperature is increased, a smaller $H_{\perp c}$ field is needed to drive the ALC/PS phases into the FE3 phase, and in

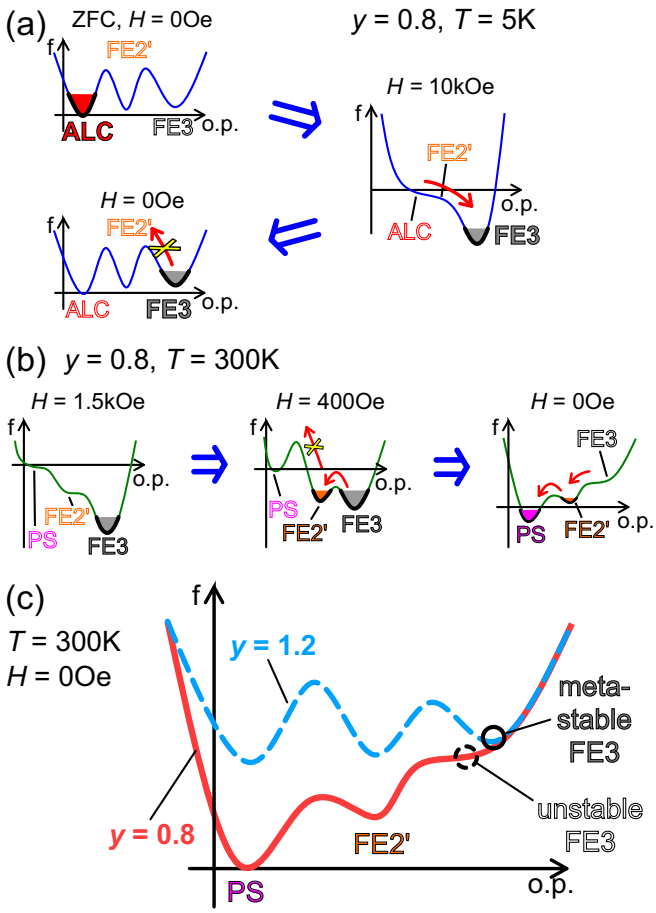

FIG. 6. (a) Metastability of the multiferroic FE3 phase exemplified for the $y = 0.8$ compound at low temperature. The alternating longitudinal conical (ALC) phase has the lowest free energy in the phase space of the order parameter (simplified as o.p. axis), therefore the ALC is stabilized by the zero-field-cooling (ZFC) process as an initial state. Application of $H_{\perp c}$ field lowers the free energy of the FE3 phase, which is stabilized and preserved when the field is removed. The FE3 phase is separated from the ALC phase by a large energy barrier and robust against thermal fluctuations. At this temperature, the FE2′ phase has a minor impact. (b) Schematic illustration of the free-energy landscape for the $y = 0.8$ compound at specific values of the $H_{\perp c}$ in the field decreasing run at 300 K. In the presence of high $H_{\perp c}$ field of 1.5 kOe, the FE3 phase is stable. At lower fields, the energy barrier between the FE3 and FE2′ phase decreases, while the barrier to the PS phase is still significant. In the absence of $H_{\perp c}$ field, the FE3 phase is unstable and disappears, while the PS phase emerges. (c) Schematic illustration of the free-energy landscape for the $y = 0.8$ and 1.2 compounds. In the $y = 0.8$ compound, the free-energy barrier between the FE3 and PS phases is more reduced than in the $y = 1.2$ due to the presence of the FE2′ phase.

turn the FE3 phase more easily returns back into the ALC/PS phases in the field-decreasing runs.

Due to several competing energies, coexisting multiferroic phases, such as FE1, FE2, FE2′, and FE3, are commonly observed in Y-type hexaferrites [5,15,23,26,36]. In this respect, Fig. 6(b) illustrate a possible interpretation for the role of the FE2′ phase, taking an example of the $y = 0.8$ compound. A moderate field of $H_{\perp c} = 1.5$ kOe stabilizes the FE3 phase at $T = 300$ K, while the FE2′ and PS phases are unstable. As the $H_{\perp c}$ field is decreased to 400 Oe, both the PS and FE2′ phases are regarded as metastable states with higher free energy than the FE3 phase. While the energy barrier between the PS and FE3 phases is still sufficiently large, the barrier between the FE2′ and FE3 phases becomes small and the FE2′ phase appears. When the $H_{\perp c}$ field is removed, the FE3 phase is destabilized, and the energy barrier between the PS and the FE2′/FE3 phases vanishes, stabilizing the PS phase. In this scenario, the FE2′ phase takes the role of an intermediate state, which bridges the FE3 and PS/ALC phases.

In the $y = 0.8$ compound, the FE2′ phase may greatly reduce the energy barrier between the FE3 and ALC phases, thereby destabilizing the FE3 phase. In the $y = 1.2$ compound, on the contrary, the energy landscape changes and the metastability of the FE3 phase is preserved, as schematically shown in Fig. 6(c).

IV. MAGNETIZATION-POLARIZATION COUPLING IN EXTERNAL FIELDS

The existence of a stable multiferroic phase is a necessary condition for the E-field control of the ferromagnetic moment, however it is not yet a sufficient one, as discussed for Z-type hexaferrites as an example in the Introduction. In multiferroic compounds, magnetoelectric domains can form where the M and P have different coupling, say $\tau = +1$ or -1 coupling as exemplified for Y-type hexaferrites in Figs. 1(b) and 1(c). These states have the same energy in the absence of external fields, and show responses with opposite sign to the external field. Therefore, in a multidomain sample, the overall magnetoelectric response is compensated. Application of external E and H fields (magnetoelectric poling) can stabilize one of these states, and then a finite magnetoelectric response can emerge. In addition, the magnetoelectric state has to be robust against external stimuli; namely, once a magnetoelectric state is selected, it should be hardly changed into the other state. This suggests that these states have to be well separated from each other by a large energy barrier. To understand the coupling in detail, we selectively alter the electric or magnetic energy by applying external fields, and we investigate the magnetic as well as the magnetoelectric properties.

A. Direct and converse magnetoelectric responses

First, the direct and converse magnetoelectric responses were studied using the isothermal P-H and M-H measurements, shown in Figs. 7 and S5 [38]. Both types of measurements were conducted for a single-domain magnetoelectric state, prepared by the application of large E and H fields in the $\mathbf{E} \perp \mathbf{H}$; $\mathbf{E}, \mathbf{H} \perp c$ geometry. To obtain the P-H loops, pyrocurrent was measured in the absence of E field while the H field was cyclically swept between ± 5 kOe for 17–50 times. The M-E measurements were performed after carefully removing the H field, while the E field was swept between ± 5 MV/m. As shown in Figs. 7(a)–7(f), the FE3 phase is stable at $T = 250$ K and the P-H as well as the M-E loops exhibit an antisymmetric field dependence. This demonstrates that the prepared magnetoelectric state is stable, that is, P and

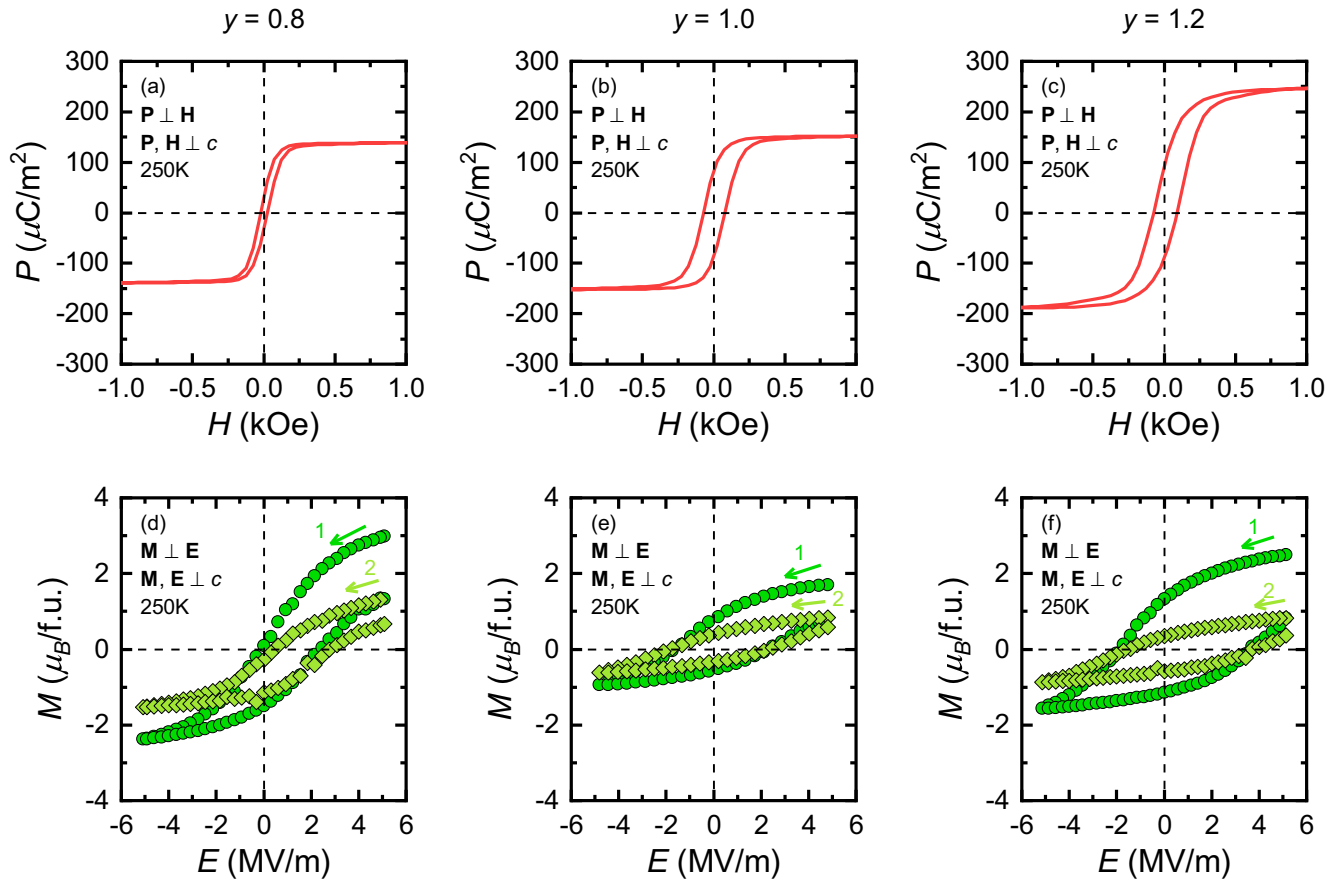

FIG. 7. The magnetoelectric responses in $Ba_{2-y}Sr_yCo_2Fe_{12-x}Al_xO_{22}$ ($x = 0.9$) are demonstrated. In (a)–(c) and (d)–(f), *P*-*H* and *M*-*E* curves at 250 K are presented. Both the *P*-*H* and *M*-*E* curves exhibit antisymmetric field dependence at this temperature. Panels (a,d), (b,e), and (c,f) correspond to the compounds with $y = 0.8$, 1.0, and 1.2, respectively.

M are strongly coupled, and the $H(E)$ field cannot change the $M(P)$ state without switching the $P(M)$ state. The saturation value of *P* depends on the Ba/Sr ratio, and it increases from $P_H^{sat} = 150\ \mu C/m^2$ for $y = 0.8$ to $P_H^{sat} = 250\ \mu C/m^2$ for $y = 1.2$. Accordingly, the *H* field needed to saturate the *P* increases from $H^{sat} = 250$ Oe for the Ba-rich compound ($y = 0.8$) to $H^{sat} = 600$ Oe in the Sr-rich compound ($y = 1.2$).

In contrast to the *P*-*H* experiments, the *M*-*E* loops are incomplete and the magnitudes of *M* decrease for every cycle of the *E* field application at 250 K. Despite the large *E* field, saturation of *M* is clearly not reached, and the samples show a characteristic feature of fatigue. Nevertheless, the largest changes in the *M* are achieved in the $y = 0.8$ and 1.2 compounds. The coercive E_C field is the smallest in the Ba-rich compound, which explains the large magnitude of the magnetization change $\Delta M_E^s = 5.5\mu_B$/f.u. for the application of ±5 MV/m fields [for the definition of ΔM_E^s, see Fig. 8(e)]. By contrast, although the E_C is the largest in the Sr-rich compound, the large magnitude of $\Delta M_E^s = 4.5\ \mu_B$/f.u. is achieved, which is rather ascribed to the stronger *P*-*M* coupling. In each compound, the remanent values of the *P* and *M* are a fraction of their respective saturation values, suggesting the formation of *P*- and *M*-domains. However, within a domain, the *P* and *M* are strongly coupled together, i.e., the *P* and *M* domain walls are confined and the magnetoelectric state is preserved, probably even within the domain walls.

Figure 8 compares the temperature dependence of representative quantities related to the magnetoelectric responses (P_H^{rem}, P_H^{sat}, ΔM_E^r, and ΔM_E^s) for all three compounds. Figure 8(a) shows the definition for the remanent value of the polarization, P_H^{rem}, while the P_H^{sat} is defined as the maximum of the *P*-*H* loops, which is different from the high-field limit. The quantity ΔM_E^r has prominent technological significance, as it measures the change in the nonvolatile *M* for the first cycle of the *E* field, as defined in Fig. 8(e). As the saturation is not reached in the *M*-*E* experiments, we can only define the change in the *M* for the application of ±5 MV/m fields, ΔM_E^s, as illustrated in Fig. 8(e). For all three compounds, P_H^{sat} as well as P_H^{rem} decrease toward higher temperatures, in contrast to ΔM_E^s and ΔM_E^r, which exhibit nonmonotonous temperature dependence. At 300 K, the *P*-*H* and *M*-*E* loops become small with saturation values of $P_H^{sat} = 10$–$50\ \mu C/m^2$ and $\Delta M_E^s = 0.25\mu_B$/f.u., respectively. The nonmonotonous behavior of ΔM_E^s and ΔM_E^r is most prominent in the case of the $y = 0.8$ compound, where these changes increase up to a maximum value of $\Delta M_E^s = 6.0\mu_B$/f.u. at $T = 240$ K, then drops to zero before reaching $T = 300$ K. The temperature dependence of ΔM_E^s and ΔM_E^r is partly ascribed to that of the coercive E_C field, shown in Figs. S7(a)–S7(c). Between $T = 200$ and 240 K, E_C decreases as *T* is increased and therefore it is easier to switch the *M* domains using *E* field. However, as the temperature is further increased, the *P*-*M*

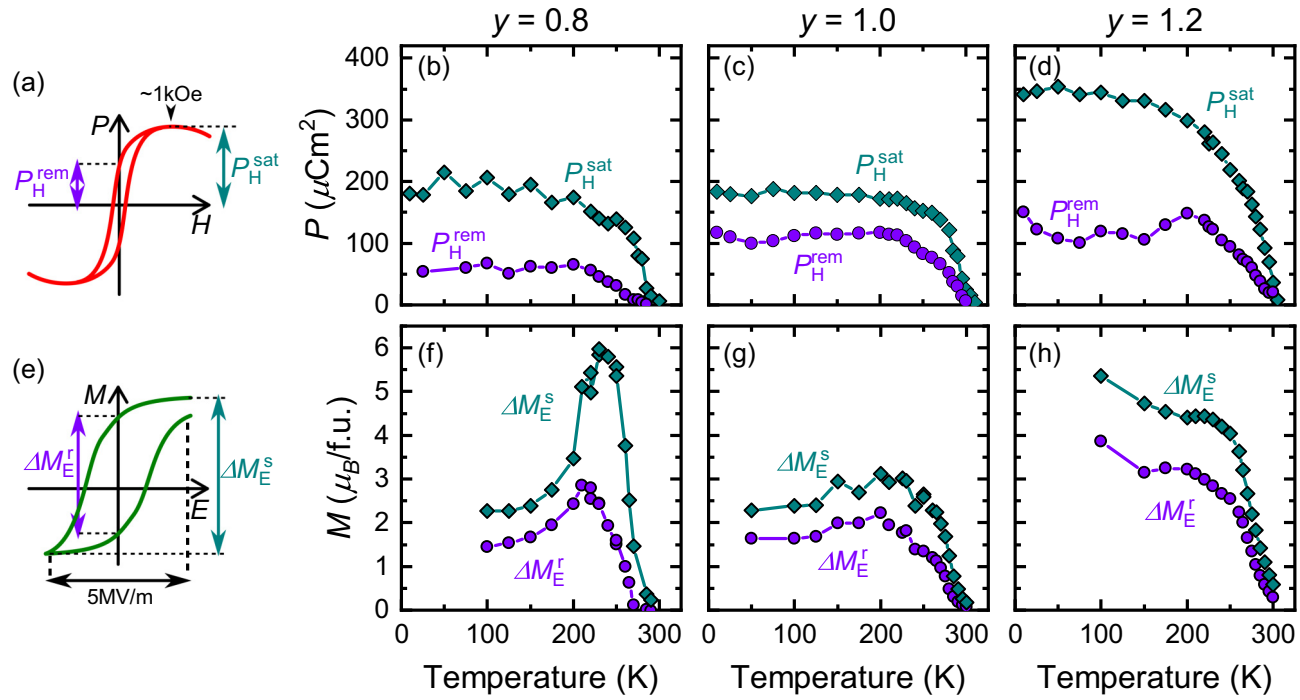

FIG. 8. (a) Schematic illustration of a P-H loop showing the definition for the saturation ($P_{\mathrm{H}}^{\mathrm{sat}}$) and remanent ($P_{\mathrm{H}}^{\mathrm{rem}}$) values of the polarization of magnetic origin. (b)–(d) Temperature dependence of $P_{\mathrm{H}}^{\mathrm{sat}}$ and $P_{\mathrm{H}}^{\mathrm{rem}}$ in the $Ba_{2-y}Sr_yCo_2Fe_{12-x}Al_xO_{22}$ ($x = 0.9$) with $y = 0.8$, 1.0, and 1.2 in panels (b), (c), and (d), respectively. Note that panels (b)–(d) share common scales for the vertical axis while the horizontal axes are the same with (f)–(h). (e) Schematic illustration of an M-E curve. The $\Delta M_{\mathrm{E}}^{\mathrm{s}}$ is defined as the magnetization change between $E = \pm 5$ MV/m fields, while $\Delta M_{\mathrm{E}}^{\mathrm{r}}$ is the change in the remanent magnetization for the first cycle of the E-field. (f)–(h) Temperature dependence of $\Delta M_{\mathrm{E}}^{\mathrm{s}}$ and $\Delta M_{\mathrm{E}}^{\mathrm{r}}$ in all three compounds shown with a common scale for the vertical axis.

coupling is lost and the $\Delta M_{\mathrm{E}}^{\mathrm{s}}$ and $\Delta M_{\mathrm{E}}^{\mathrm{r}}$ approach zero. In addition to the reduced magnitudes, the P-H and M-E loops at room temperature indicate the emergence of substantial contributions with a symmetric field dependence, i.e., the appearance of butterfly-shaped P-H and M-E curves, shown in Fig. S5. The symmetric P-H loop implies that the reversal of H field switches the magnetoelectric state, instead of the P state, hence that the magnetoelectric state is not robust against external field.

B. Magnetic phases in the presence of E and H fields

The reappearance of the incommensurate phases [proper-screw (PS) or alternating longitudinal conical (ALC)] close to room temperature is a serious issue that hinders the E-field control of the magnetization in the Y-type hexaferrite compounds. It is important to investigate the conditions with which the ALC or PS phases can be suppressed. Figure 9(a) compares the M-H loops for the $y = 1.0$ sample in multi- and single-domain magnetoelectric states at $T = 275$ K. The multidomain state (orange curve) is obtained by heating the sample up to $T = 380$ K and then cooling in zero field. The M-H curve starts from the ALC phase at 0 kOe (1) with a low initial slope of M. In agreement with the former measurements shown in Fig. 5, the ALC phase is replaced by the FE3 phase around 0.9 kOe, which is signaled by a jump in the M. When the H field is swept back and reversed (2), the ALC phase partially reemerges around −0.15 kOe and again vanishes around −0.9 kOe. In the second field-increasing run (3), the reemergence of the ALC phase in the positive low-H region is observed. Next, the single-domain magnetoelectric state is prepared by the application of large poling E and H fields ($E_0 = +5$ MV/m, $H_0 = +50$ kOe) in the $\mathbf{E} \perp \mathbf{H}$; $\mathbf{E}, \mathbf{H} \perp c$ geometry at 275 K, and the M-H measurement is started from a high H field in the absence of E field (black dashed curve). In this case, the ALC phase with small magnetization is not observed, while the FE3 phase is preserved throughout the M switching process. Thus, in the single-domain magnetoelectric-state, the formation of nonmagnetoelectric phases is greatly suppressed.

A possible explanation for these features is schematically illustrated in Fig. 9(b). In the sample without magnetoelectric poling, there are many domain boundaries in contrast to the poled case. At the magnetoelectric domain walls, the P forms a head-to-head or tail-to-tail configuration with increased electrostatic energy, which may serve as a seed for the formation of the nonpolar ALC phase, in accordance with the observation by recent studies [29,41]. In the multidomain magnetoelectric-state, the ALC domains can expand into a macroscopic phase, while in the single-domain case there is no such domain wall to be a seed for the ALC phase. Further differences of magnetic properties between the multi- and single-domain magnetoelectric-states are illustrated in Figs. S7(d)–S7(i) for all three materials.

When the E and H fields are simultaneously applied for coupled P-M domains of a multiferroic material, E-field biasing for the M-H hysteresis loop can be observed [22,42,43].

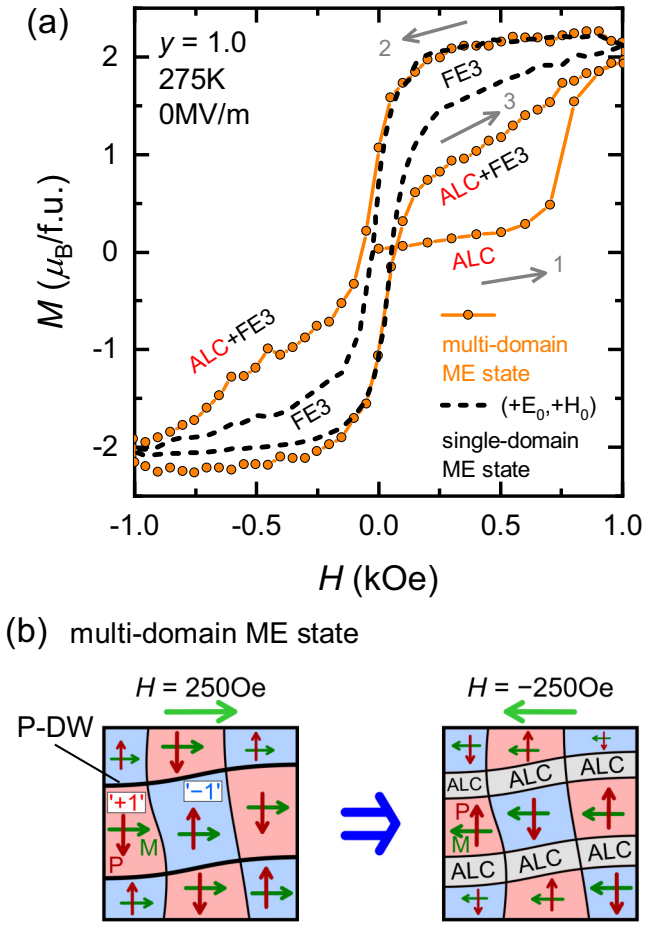

FIG. 9. (a) Magnetization curves of the $y = 1.0$ sample in multi- and single-domain magnetoelectric (ME) states taken in the absence of E-field. Without magnetoelectric poling, the ALC phase reappears just after the sign reversal of the H-field (orange curve). In the single-ME-domain case, the FE3 phase is preserved throughout the experiment (black, dashed curve). The single-domain state was prepared by applying $E_0 = +5$ MV/m, $H_0 = +50$ kOe fields. (b) Schematic illustration of the multidomain ME state within the ab plane upon the reversal of the in-plane H field. The red and blue regions correspond to the $\tau = +1$ and -1 ME states of the FE3 phase, respectively. P-DW denotes the polarization domain walls. The alternating longitudinal conical (ALC) phase is shown as a gray area in the right panel. Green and red arrows indicate the direction of M and P, respectively. The ALC phase can form at the edges of the magnetoelectric domains, where P can be zero to reduce the electrostatic energy originating from the head-to-head or tail-to-tail configuration. In the multidomain case, the ALC phase can readily expand into macroscopic domains. In the single-domain state, the ALC phase is difficult to nucleate.

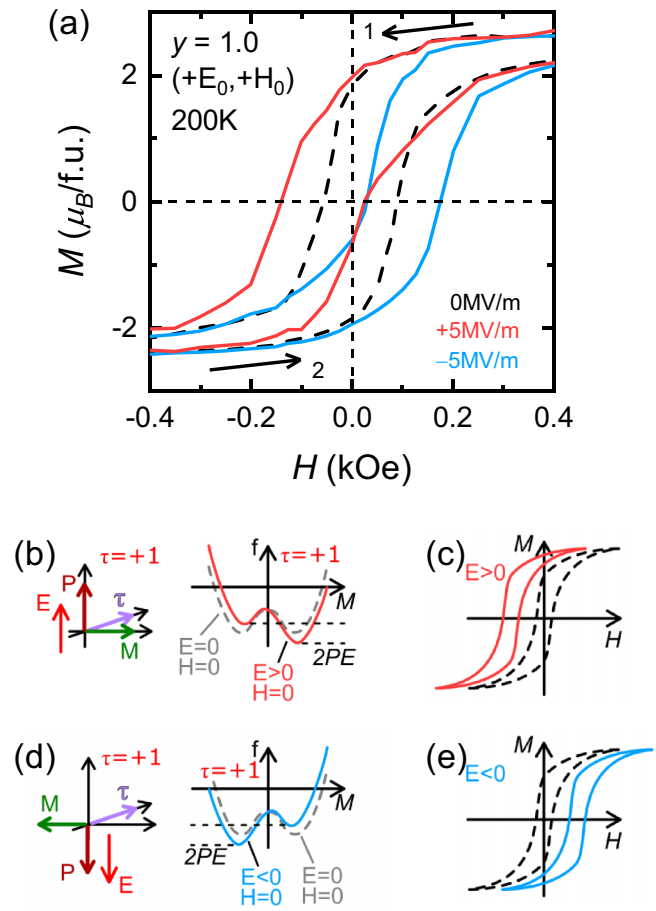

FIG. 10. (a) E-field biased M-H measurements on a sample with $y = 1.0$ in a single-domain magnetoelectric-state, prepared by $E_0 = +5$ MV/m, $H_0 = +50$ kOe poling fields at $T = 200$ K. (b)–(e) Schematic illustration of the E-field biased M-H measurements on a sample in the $\tau = +1$ magnetoelectric state. (b) In the presence of $E > 0$ field, the free energy of the $+P$ and therefore the $+M$ states is lowered. Hence, the $+M$ state is more stable than the $-M$ state even in the absence of H-field. (c) As larger negative field is needed for the M switching to compensate the electrostatic energy, the M-H hysteresis is shifted to the $-H$ direction. (d) In the presence of $E < 0$ field, the free energy of the state with $-P$ and $-M$ is lowered. (e) In this case, the M-H hysteresis is shifted toward the $+H$ direction.

In Fig. 10, we demonstrate this effect for the $y = 1.0$ sample at $T = 200$ K. The fields were applied in the $\mathbf{E} \perp \mathbf{H}$ and $\mathbf{E}, \mathbf{H} \perp c$ geometry. Prior to the M-H measurements, the sample was poled into a single-domain $\tau = +1$ magnetoelectric state using $(+E_0, +H_0)$ fields ($E_0 = 5$ MV/m, $H_0 = 50$ kOe). When no E field is applied, the M-H loop of the single-domain sample is centered at $H = 0$ (dashed black curve), as shown in Fig. 10(a). Upon applying $E > 0$ (red curve) or $E < 0$ (blue curve) fields, the M-H loop shifts toward the $-$ or $+$ direction of the H-field axis, respectively. A schematic explanation for the E-biased M-H loop is provided in Figs. 10(b)–10(e). In the $\tau = +1$ state, the $+P$ and $-P$ states are clamped with the $+M$ and $-M$ magnetic states, respectively. In the presence of $E > 0$ field, the $(+P, +M)$ state has a lower free energy by $2\,PE$ in the absence of H field, as shown in Fig. 10(b). When the coupling is strong, P and M cannot be switched independently. To switch the magnetic state, the dielectric part of the free energy $2\,PE$ has to be compensated by the application of a larger coercive field $H_C(E)$. Therefore, the M-H loop is shifted to the $-H$ direction [Fig. 10(c)]. On the contrary, when an $E < 0$ field is applied, the free energy of the $(+P, +M)$ state is higher by $2\,|PE|$, and the M-H loop is shifted to the $+H$ direction, as shown in Figs. 10(d) and 10(e).

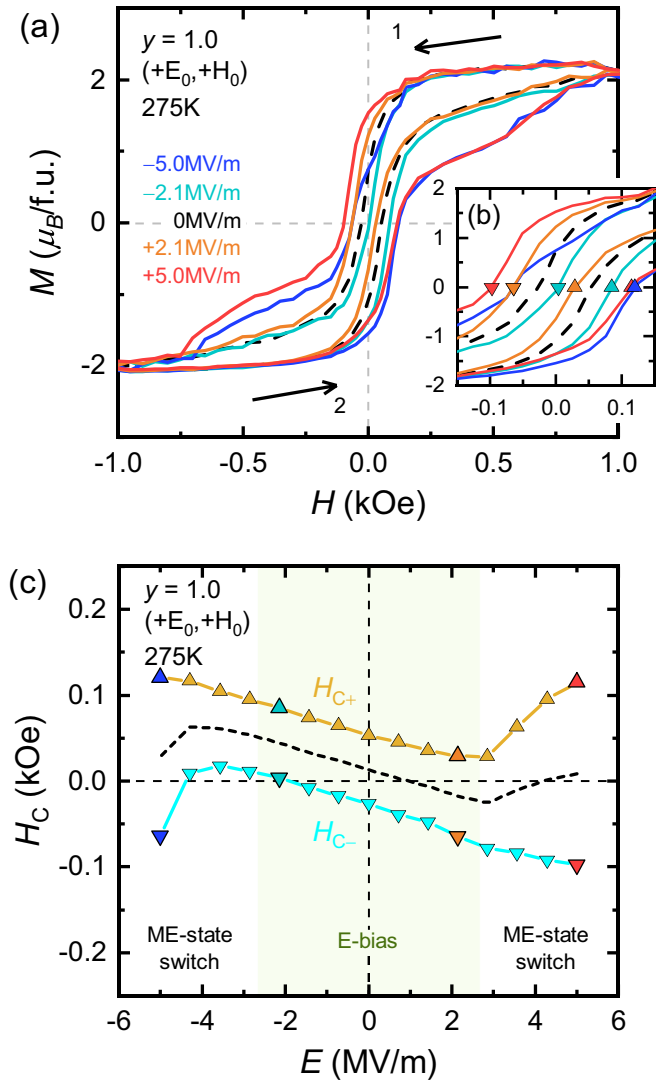

FIG. 11. (a) Magnetization curves of the $y = 1.0$ sample at $T = 275$ K in the presence of several E fields. The measurement was started from the single-domain magnetoelectric state, attained by $E_0 = +5$ MV/m, $H_0 = +50$ kOe poling fields. (b) Expanded view of the M-H loops of panel (a). The upward (downward) triangles indicate the H_{C+} (H_{C-}) coercive fields in the field-increasing (decreasing) runs. (c) Electric-field dependence of H_{C+} and H_{C-} coercive fields. Black dashed line indicates the average of H_{C+} and H_{C-}. For $|E| < 3$ MV/m fields, the coercive fields show a linear E-field dependence. For larger E fields, H_C deviates from the linear relation, indicating that the magnetoelectric state is switched. In addition, the ALC phase reappears during the field-sweeping [see panel (a)].

At low temperatures, the magnetic coercive fields H_{C+} and H_{C-} for the H-increasing and -decreasing runs, respectively, exhibit a linear E-field dependence, as shown in Fig. S8. At high temperatures, however, the $H_{C\pm}(E)$ coercive fields show a more complex E-field dependence. Figures 11(a) and 11(b) display E-field biased M-H loops measured at $T = 275$ K, while the E-field dependence of the $H_{C\pm}$ is presented in Fig. 11(c). The measurements were started from the single-domain $\tau = +1$ magnetoelectric state, similarly to the earlier cases. As shown in Fig. 11(c), when the magnitude of the E field is small, the M-H hysteresis loops are shifted in proportion to the applied E field, in the same way as the low-temperature measurements presented in Figs. 10 and S8. However, when large E fields are applied, the linear dependence of $H_{C\pm}$ on E-field does not hold anymore, and the hysteresis loop is widened instead of shifted. Besides, as indicated by shoulderlike structures at $0.2 \leqslant |H| \leqslant 0.8$ kOe, the ALC phase reappears even when the sample was initially poled to a single-domain magnetoelectric state, in contrast to the case shown with a dashed line in Fig. 9(a). The widening of the hysteresis loop, and hence the deviation of $H_{C\pm}(E)$ from linear dependence, suggests the switching between the $\tau = +1$ and -1 states. In the presence of $E > 0$ and $H < 0$ fields with high absolute values, the original $\tau = +1$ state is turned into the $\tau = -1$ state to gain both the electrostatic energy and the Zeeman energy. Therefore, in the subsequent H-increasing run from negative to positive field, the H_{C+} is shifted to larger positive fields due to the reversed P-M coupling. The reemergence of the nonpolar ALC/PS phases in the presence of E and H fields is more clearly demonstrated in Fig. S9.

C. Investigation of the P-M coupling

The switching between the $\tau = +1$ and -1 magnetoelectric states in the E-field biased M-H measurements at high temperatures (Fig. 11) motivated us for further experiments, namely E-field biased P-H measurements. This experiment may provide more reliable information on the P-M coupling than the differential magnetoelectric susceptibilities, often used in the literature [11,12,15,20,21]. In multiferroic materials, the differential magnetoelectric susceptibilities, defined as $\partial P/\partial H$ and $\partial M/\partial E$, are dominated by domain switching effects at low fields, similar to the $\partial M/\partial H$ susceptibility in ferromagnets.

Figures 12(a) and 12(b) show P-H loops for $y = 1.2$ at $T = 200$ K with a complete cycle of the H-field for two different values of the applied E field. The E and H fields are in the $\mathbf{E} \perp \mathbf{H}$ and $\mathbf{E}, \mathbf{H} \perp c$ configuration. In Fig. 12(a), the measurement is started from $H = +60$ kOe in the collinear FiM phase (where P is zero), in the presence of a small $E = +0.5$ MV/m field. As the H field is decreased below $H = +42$ kOe to enter into the FE3 phase, the sample is poled to a single-domain magnetoelectric state with $\tau = +1$, and $P > 0$ emerges. When the H field is reversed to negative, the M as well as the coupled P is reversed to negative, while keeping the $\tau = +1$ state. As the field approaches $H = -42$ kOe, the FE3 phase is turned again into the FiM phase and the field-induced P vanishes. When the H field is increased from negative to positive, a similar P-H curve is observed with the opposite sign to that of P, as in this case the combination of $E > 0$ and $H < 0$ fields selects the $\tau = -1$ magnetoelectric state; the FE3 phase reappears at $H = -42$ kOe with positive P, which is reversed to negative at $H = 0$ kOe and disappears again at $H = 42$ kOe field.

However, in the presence of high $E = +4.5$ MV/m field, the P-H loop exhibits different behavior, as shown in Fig. 12(b). In the field-decreasing run, after the P is once switched to negative around $H = 0$, the P is switched back to positive within the FE3 phase before reaching the FE3-FiM

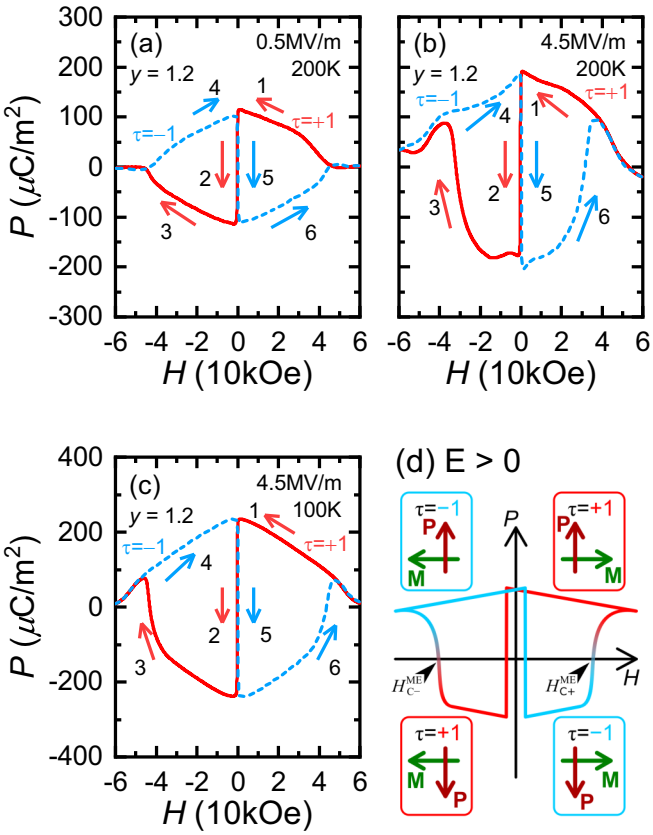

FIG. 12. (a,b) Magnetic-field dependence of polarization (P-H) for $y = 1.2$ compound at $T = 200$ K in the presence of $E = 0.5$ and 4.5 MV/m in panels (a) and (b), respectively. The numbered arrows indicate the sequence of the measurement, starting from the FiM phase at $H = 60$ kOe. (c) P-H loop measured in the presence of $E = 4.5$ MV/m field at $T = 100$ K. (d) Schematic illustration of a P-H hysteresis loop in the presence of large E (> 0) field. Simultaneous application of large E and H fields switches the magnetoelectric state between $\tau = +1$ and -1. The coercive fields $H_{C\pm}^{ME}$ correspond to the H field needed to switch between the $\tau = +1$ and -1 states for a given value of the E field.

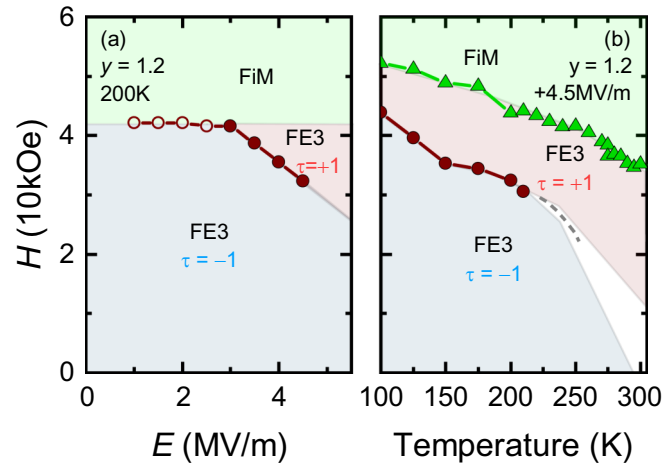

FIG. 13. (a) The H-E phase diagram for $y = 1.2$ compound at $T = 200$ K, showing the $\tau = -1$ and $+1$ magnetoelectric states of the FE3 phase as well as the ferrimagnetic (FiM) phase. Data points are taken in the H-increasing run from -60 to $+60$ kOe in the presence of positive E-fields. Open and full symbols correspond to partial and complete switching between the magnetoelectric states. The boundary separating the $\tau = -1$ and $+1$ states has a strong E-dependence for the high-field region, while the FiM-FE3 phase boundary is independent of the E-field. (b) The H-T phase diagram showing the $\tau = -1$ and $+1$ states of the FE3 phase and the FiM phase in the presence of the $E = 4.5$ MV/m field determined in the H-increasing runs at each temperature. The boundary between the $\tau = -1$ and $+1$ states is the E-dependent coercive field H_C^{ME} needed to switch between the magnetoelectric states.

phase boundary. This corresponds to the magnetoelectric state switching from $\tau = +1$ to -1. The isothermal switching between the $\tau = +1$ and -1 states is more clearly demonstrated in Fig. 12(c) at a lower temperature, $T = 100$ K; a schematic illustration for the switching process is provided in Fig. 12(d).

Similar measurements at 200 K with changing the E field reveal a first-order boundary between the two magnetoelectric states of the FE3 phase, as shown in Fig. 13(a). The coercive field H_C^{ME} corresponds to the switching from the $\tau = -1$ to $+1$ state for a given value of the E field [for definition, see the caption of Fig. 12(d)]. At $T = 200$ K, $E < 3$ MV/m field is insufficient and results in partial switching, i.e., only a tiny portion is reversed in terms of the magnetoelectric state. For higher E fields, the H_C^{ME} decreases.

Figure 13(b) shows the temperature dependence of the coercive field H_C^{ME} in the H-increasing run for an applied E-field of $+4.5$ MV/m. The displacement current measurement under such a high E-field is possible only up to $T = 220$ K, above which the current peaks of magnetic origin are masked out by large background noise. For comparison, the FE3-FiM phase boundary is also shown in the H-increasing runs. It is noted that the H_C^{ME} may be affected by domain-pinning effects, as well as by the proximity to the FiM phase. The H_C^{ME} field monotonously decreases toward higher temperatures. This means that as the temperature is elevated, the $\tau = +1$ magnetoelectric states can be switched by the application of both smaller E and H fields, and that they are fragile against external stimuli and thermal agitation. This accounts for the observed P-H loops with increased contribution from a symmetric component, as shown in Fig. S5.

The connection between the P-M coupling and the $H_C^{ME}(E)$ field is discussed in Fig. 14(a). The $\tau = +1$ and -1 states can also be described in terms of φ^S as $\varphi^S > 0$ and $\varphi^S < 0$, respectively, shown in Fig. 1(b). In the absence of external fields, the two magnetoelectric states have the same free energy and they are separated by an energy barrier. In the presence of H-field [$H > H_C^{ME}(E)$] shown in Fig. 14(a), the energy barrier is reduced, and one of the magnetoelectric states is selected according to the sign of the E and H fields (poling process). In this sense, the $H_C^{ME}(E)$ is related to the energy barrier separating the $\tau = +1$ and -1 states and is considered to be an appropriate measure for the P-M coupling.

To understand the mechanism of the switching of P-M clamping, we discuss the role of domain walls. When the external E or H field is reversed, the new majority domains expand, and P- or M-domain walls propagate throughout the

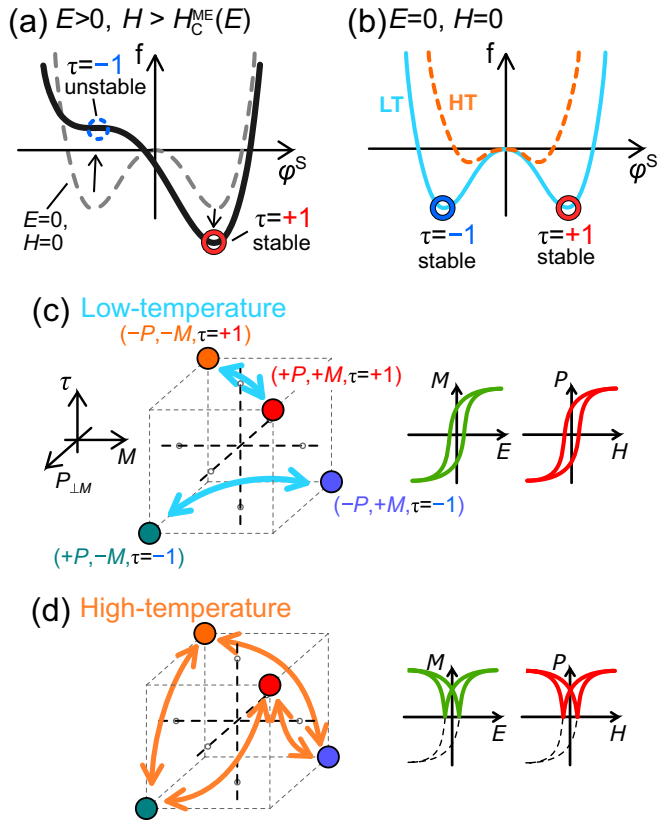

FIG. 14. (a) Free energy of the FE3 phase as a function of the canting angle of the S^S block spin. In the absence of E and H fields, free energies for the $\tau = +1$ and -1 states are degenerate (dashed curve). When large E and H fields are applied($H > H_C^{ME}(E)$) simultaneously, the free-energy barrier vanishes, and the $\tau = +1$ state is stabilized, while the $\tau = -1$ state is destabilized. (b) Schematic illustration of the free-energy landscape showing the $\tau = +1$ and -1 states of the FE3 phase at low (LT) and high (HT) temperatures. The magnetic state is described by the φ^S angle, and the states are separated by a free-energy barrier. At low temperature, the energy barrier is large and the magnetoelectric states are robust. At high temperatures, the energy barrier is small and the magnetoelectric state can be switched easily. (c) Order parameter phase space spanned by P, M, and τ axes (left). At low temperatures, the P-M coupling is strong, and once a magnetoelectric state is selected ($\tau = +1$ or -1) by the poling E and H fields, it is preserved. Then, the magnetoelectric response, i.e., the M-E and P-H curves, show an antisymmetric field dependence (right). (d) At high temperatures, the P-M coupling is weak and the initial states are not preserved. Hence, switching between $\tau = +1$ and -1 states occurs as indicated by orange arrows. The switching between the states results in the symmetric magnetoelectric response, i.e., symmetric M-E and P-H loops as shown in the right panel.

sample. In the absence of P-M coupling, these domain walls are independent and propagate separately. The P-M coupling governs the possible types of domain walls, and in the limit of strong coupling, only combined multiferroic domain walls are allowed [44]. In the present Y-type hexaferrites, the multiferroic domain walls are considered to be composed of simultaneously rotating P and M around the c axis while keeping their relative configuration unchanged [28,29]. However, when the combined domain walls with moderate coupling propagate through pinning centers or defects, the P- and M-domain walls may get deconfined from each other, and one of the two magnetoelectric states can be converted into another. This situation is microscopically different from, yet bears some resemblance to, the simultaneous application of E and H fields. At low temperature, the spin-canting angles φ^S and φ^L, and hence the energy barrier between the $\tau = +1$ and -1 states, is large [Fig. 14(b)], and the switching between them cannot occur. The P- and M-domain walls are confined, and the magnetoelectric response is antisymmetric, as observed in Fig. 5 and also schematically shown in Fig. 14(c). However at high temperatures, φ^S and φ^L, and hence the energy barrier separating the two states becomes small and can be overcome by the increased thermal agitation. In this case, the P- and M-domain walls are deconfined, making the magnetoelectric effect symmetric, as shown in Figs. S5 and 14(d).

V. SUMMARY

We have investigated the systematic change in the stability of several competing magnetic phases in the Y-type hexaferrites $Ba_{2-y}Sr_yCo_2Fe_{12-x}Al_xO_{22}$ ($x = 0.9$) by changing the Ba/Sr ratio from $y = 0.8$ to 1.2. The H-T phase diagram that depends on the field history was studied by using magnetization, electric polarization, and neutron diffraction measurements for single-crystal samples grown by the laser floating zone method (see Figs. 1-5, and Sec. III D). The resistive properties of the synthesized crystals were much improved by the application of the oxygen annealing procedure to allow the polarization measurements at high temperatures up to room temperature.

As a generic feature, these materials host the nonpolar alternating longitudinal conical (ALC) and proper-screw (PS) phases in their zero-field-cooled state (see Fig. 1). Upon applying the H-field perpendicular to the c axis ($H_{\perp c}$), a multiferroic phase endowed with magnetoelectric functions, termed the FE3 phase, emerges. In our study, we found that the stability of the FE3 phase is improved as the Sr-doping level is increased (shown in Fig. 4). In the Ba-rich compound ($y = 0.8$), the FE3 phase is unstable and turns into the ALC phase when the $H_{\perp c}$ field is removed at room temperature. In the compound with an equal amount of Ba and Sr ($y = 1.0$), the FE3 phase is partially preserved in the absence of the $H_{\perp c}$ field after once applied. The FE3 phase is found to be most stable in the Sr-rich compound ($y = 1.2$) among the three compounds investigated in this study. This phase emerges with other coexisting phases in the zero-field-cooled state but fully preserved below $T = 280$ K when the $H_{\perp c}$ field is applied and even after $H_{\perp c}$ is removed. It appears that the stability of the FE3 phase and interplay between the FE3 and ALC phases are influenced by a third magnetic phase, termed the FE2′ phase. The FE2′ phase may be regarded as an intermediate state, which likely promotes the conversion between the FE3 and ALC magnetic orders. We discussed these findings in Sec. III D by using schematic illustrations for possible free-energy diagrams. We note that the free-energy diagrams are introduced phenomenologically, based on the magnetization and neutron diffraction data and not on actual calculations.

For the successful reversal of M by E-field, the existence of a stable multiferroic phase is necessary, but not sufficient. In some materials with symmetric magnetoelectric responses, the M does not change sign upon the reversal of E-field, and instead the magnetoelectric state is switched (see Figs. 7 and 8). This means that the free-energy barrier separating the different states of the magnetoelectric phase has to be sufficiently large, in addition to those between the multiferroic phase and the nonpolar magnetic phases. We addressed these issues by selectively changing the electric and magnetic state with the application of large E and H fields for the samples in both multi- and single-domain magnetoelectric states. We found that the formation of the ALC phase is greatly suppressed in the single-domain magnetoelectric samples, which points to the importance of domain boundaries or walls in the phase conversion mechanism in these materials (see Fig. 9). The P-M coupling was also studied by measuring the temperature dependence of the coercive fields, across which the two magnetoelectric states of the FE3 phase are switched to one another (shown in Figs. 10–14 and Sec. IV C).

Magnetization switching by E-field in the Y-type hexaferrites is realized by the propagation of complex P- and M-domain walls with some mutual coupling [29]. When the canting angle of the block-spin, and hence the energy barrier between the two magnetoelectric states of the FE3 phase, is small, thermal agitation deconfines the P- and M-domain walls, leading to butterfly-shaped M (see Fig. 14). In addition, when the energy barrier between the magnetoelectric and nonpolar phases is small, the FE3 phase is turned into the ALC or PS phases, resulting in the complete loss of P-M coupling. Therefore, the double-fan structure of the FE3 phase has to be robust against thermal agitation and other perturbations for the enhanced P-M coupling. To keep the FE3 structure robust, the strength of the exchange interactions among the S^{S} and S^{L} spin-blocks has to be increased, while the anisotropy within the ab plane is further reduced.

ACKNOWLEDGMENTS

The authors are grateful for the fruitful discussion with Nicola Spaldin and Naoto Nagaosa. This research used resources at the High Flux Isotope Reactor, a DOE Office of Science User Facility operated by the Oak Ridge National Laboratory. This research was supported in part by the U.S.-Japan Cooperative Program on Neutron Scattering. The structural unit cell of the Y-type hexaferrite crystal was illustrated using the software VESTA [45].

[1] T. Kimura, T. Goto, H. Shintani, K. Ishizaka, T. Arima, and Y. Tokura, Nature (London) **426**, 55 (2003).
[2] N. Hur, P. A. Sharma, J. S. Ahn, S. Guha, and S.-W. Cheong, Nature (London) **429**, 392 (2004).
[3] N. A. Spaldin and M. Fiebig, Science **309**, 391 (2005).
[4] T. Kimura, G. Lawes, and A. P. Ramirez, Phys. Rev. Lett. **94**, 137201 (2005).
[5] S. Ishiwata, Y. Taguchi, H. Murakawa, Y. Onose, and Y. Tokura, Science **319**, 1643 (2008).
[6] S. Fusil, V. Garcia, A. Barthélémy, and M. Bibes, Annu. Rev. Mater. Res. **44**, 91 (2014).
[7] D. Khomskii, Physics **2**, 20 (2009).
[8] H. Katsura, N. Nagaosa, and A. V. Balatsky, Phys. Rev. Lett. **95**, 057205 (2005).
[9] C. Jia, S. Onoda, N. Nagaosa, and J. H. Han, Phys. Rev. B **74**, 224444 (2006).
[10] C. Jia, S. Onoda, N. Nagaosa, and J. H. Han, Phys. Rev. B **76**, 144424 (2007).
[11] J. Wang, J. B. Neaton, H. Zheng, V. Nagarajan, S. B. Ogale, B. Liu, D. Viehland, V. Vaithyanathan, D. G. Schlom, U. V. Waghmare, N. A. Spaldin, K. M. Rabe, M. Wuttig, and R. Ramesh, Science **299**, 1719 (2003).
[12] J. T. Heron, J. L. Bosse, Q. He, Y. Gao, M. Trassin, L. Ye, J. D. Clarkson, C. Wang, J. Liu, S. Salahuddin, D. C. Ralph, D. G. Schlom, J. Iniguez, B. D. Huey, and R. Ramesh, Nature (London) **516**, 370 (2014).
[13] M. Tokunaga, M. Akaki, T. Ito, S. Miyahara, A. Miyake, H. Kuwahara, and N. Furukawa, Nat. Commun. **6**, 5878 (2015).
[14] Y. Kitagawa, Y. Hiraoka, T. Honda, T. Ishikura, H. Nakamura, and T. Kimura, Nat. Mater. **9**, 797 (2010).
[15] S. H. Chun, Y. S. Chai, Y. S. Oh, D. Jaiswal-Nagar, S. Y. Haam, I. Kim, B. Lee, D. H. Nam, K.-T. Ko, J.-H. Park, J.-H. Chung, and K. H. Kim, Phys. Rev. Lett. **104**, 037204 (2010).
[16] T. Kimura, Annu. Rev. Condens. Matter Phys. **3**, 93 (2012).
[17] V. Kocsis, Y. Tokunaga, S. Bordács, M. Kriener, A. Puri, U. Zeitler, Y. Taguchi, Y. Tokura, and I. Kézsmárki, Phys. Rev. B **93**, 014444 (2016).
[18] Y. S. Chai, S. H. Chun, J. Z. Cong, and K. H. Kim, Phys. Rev. B **98**, 104416 (2018).
[19] H. Ueda, Y. Tanaka, Y. Wakabayashi, and T. Kimura, Phys. Rev. B **100**, 094444 (2019).
[20] Y. S. Chai, S. Kwon, S. H. Chun, I. Kim, B.-G. Jeon, K. H. Kim, and S. Lee, Nat. Commun. **5**, 4208 (2014).
[21] K. Zhai, Y. Wu, S. Shen, W. Tian, H. Cao, Y. Chai, B. C. Chakoumakos, D. Shang, L. Yan, F. Wang, and Y. Sun, Nat. Commun. **8**, 519 (2017).
[22] K. Zhai, Y. Chai, J. Cong, D. Shang, and Y. Sun, Phys. Rev. B **98**, 144405 (2018).
[23] S. Ishiwata, Y. Taguchi, Y. Tokunaga, H. Murakawa, Y. Onose, and Y. Tokura, Phys. Rev. B **79**, 180408(R) (2009).
[24] Y. Hiraoka, H. Nakamura, M. Soda, Y. Wakabayashi, and T. Kimura, J. Appl. Phys. **110**, 033920 (2011).
[25] H. B. Lee, S. H. Chun, K. W. Shin, B.-G. Jeon, Y. S. Chai, K. H. Kim, J. Schefer, H. Chang, S.-N. Yun, T.-Y. Joung, and J.-H. Chung, Phys. Rev. B **86**, 094435 (2012).
[26] H. Chang, H. B. Lee, Y.-S. Song, J.-H. Chung, S. A. Kim, I. H. Oh, M. Reehuis, and J. Schefer, Phys. Rev. B **85**, 064402 (2012).
[27] S. Hirose, K. Haruki, A. Ando, and T. Kimura, Appl. Phys. Lett. **104**, 022907 (2014).
[28] T. Nakajima, Y. Tokunaga, M. Matsuda, S. Dissanayake, J. Fernandez-Baca, K. Kakurai, Y. Taguchi, Y. Tokura, and T.-h. Arima, Phys. Rev. B **94**, 195154 (2016).

[29] V. Kocsis, T. Nakajima, M. Matsuda, A. Kikkawa, Y. Kaneko, J. Takashima, K. Kakurai, T. Arima, F. Kagawa, Y. Tokunaga, Y. Tokura, and Y. Taguchi, Nat. Commun. **10**, 1247 (2019).
[30] Y. Kaneko and Y. Tokura, J. Cryst. Growth **533**, 125435 (2020).
[31] Y. Inaguma, T. Katsumata, R. Wang, K. Kobashi, M. Itoh, Y.-J. Shan, and T. Nakamura, Ferroelectrics **264**, 127 (2001).
[32] J. Smit and H. P. J. Wijn, *Ferrites* (Philips Research Laboratories, Eindhoven (Holland), 1959).
[33] N. Momozawa, Y. Yamaguchi, H. Takei, and M. Mita, J. Phys. Soc. Jpn. **54**, 771 (1985).
[34] N. Momozawa and Y. Yamaguchi, J. Phys. Soc. Jpn. **62**, 1292 (1993).
[35] S. Utsumi, D. Yoshiba, and N. Momozawa, J. Phys. Soc. Jpn. **76**, 034704 (2007).
[36] S. Ishiwata, D. Okuyama, K. Kakurai, M. Nishi, Y. Taguchi, and Y. Tokura, Phys. Rev. B **81**, 174418 (2010).
[37] H. B. Lee, Y.-S. Song, J.-H. Chung, S. H. Chun, Y. S. Chai, K. H. Kim, M. Reehuis, K. Prokeš, and S. Mat'aš, Phys. Rev. B **83**, 144425 (2011).
[38] See Supplemental Material at http://link.aps.org/supplemental/10.1103/PhysRevB.101.075136 for further magnetization, polarization, and neutron diffraction measurements.
[39] M. Mostovoy, Phys. Rev. Lett. **96**, 067601 (2006).
[40] I. A. Sergienko and E. Dagotto, Phys. Rev. B **73**, 094434 (2006).
[41] E. Hassanpour, M. C. Weber, A. Bortis, Y. Tokunaga, Y. Taguchi, Y. Tokura, A. Cano, T. Lottermoser, and M. Fiebig, arXiv:1908.06876.
[42] K. Kimura, H. Nakamura, S. Kimura, M. Hagiwara, and T. Kimura, Phys. Rev. Lett. **103**, 107201 (2009).
[43] Y. Tokunaga, Y. Taguchi, T. Arima, and Y. Tokura, Phys. Rev. Lett. **112**, 037203 (2014).
[44] Y. Tokunaga, N. Furukawa, H. Sakai, Y. Taguchi, T.-h. Arima, and Y. Tokura, Nat. Mater. **8**, 558 (2009).
[45] K. Momma and F. Izumi, J. Appl. Crystallogr. **41**, 653 (2008).